Title: Idiosyncratic epistasis leads to global fitness-correlated trends

Authors: Christopher W. Bakerlee^{†,1,2,3}, Alex N. Nguyen Ba^{†,1,2,4}, Yekaterina Shulgina³, Jose I. Rojas Echenique^{1,6}, and Michael M. Desai^{*,1,2,5,7}

Affiliations:

- ¹Department of Organismic and Evolutionary Biology, Harvard University; Cambridge, MA, USA.
- ²Quantitative Biology Initiative, Harvard University; Cambridge, MA, USA.
- ³Department of Molecular and Cellular Biology, Harvard University; Cambridge, MA, USA.
- ⁴Department of Cell and Systems Biology, University of Toronto; Toronto, Canada.
- ⁵NSF-Simons Center for Mathematical and Statistical Analysis of Biology, Harvard University; Cambridge, MA, USA.
 - ⁶Department of Molecular Genetics, University of Toronto; Toronto, Canada.
 - ⁷Department of Physics, Harvard University; Cambridge, MA, USA.

- [†]These authors contributed equally to this work
- *Corresponding author. Email: mdesai@oeb.harvard.edu

Abstract: Epistasis can dramatically affect evolutionary trajectories. In recent decades, protein-level fitness landscapes have revealed extensive idiosyncratic epistasis among specific mutations. In contrast, other work has found ubiquitous and apparently non-specific patterns of global diminishing-returns and increasing-costs epistasis among mutations across the genome. Here, we use a hierarchical CRISPR gene drive system to construct all combinations of 10 missense mutations from across the genome in budding yeast and measure their fitness in six environments. We show that the resulting fitness landscapes exhibit global fitness-correlated trends, but that these trends emerge from specific idiosyncratic interactions. We thus provide experimental validation of recent theoretical work that has argued that fitness-correlated trends can emerge as the generic consequence of idiosyncratic epistasis.

One-Sentence Summary: A genome-spanning fitness landscape reveals how idiosyncratic genetic interactions lead to global epistatic patterns.

Main Text: Epistatic interactions have important consequences for the design and evolution of genetic systems (I-3). Significant work in recent decades has studied these interactions by measuring empirical fitness landscapes, most often at "shallow" depth for genome-scale studies (e.g., by quantifying pairwise but not higher order epistasis between all gene deletions or mutations) or at "narrow" breadth (such as complete landscapes at the scale of small select regions in single genes, for example by quantifying all orders of epistatic interactions among few amino acid residues) (4-18). These studies have often found many epistatic interactions among specific mutations at both lower (i.e., among few mutations) and higher orders (i.e., among many mutations). These reflect particular biological and physical interactions among the mutations involved; following recent work (19, 20) we refer to them as "idiosyncratic" epistasis, as they involve the specific details of these mutations. Overall, this body of work has highlighted the potential for epistasis to create historical contingency that tightly constrains the distribution of adaptive trajectories accessible to natural selection.

In contrast, other work examining adaptive trajectories that implicate loci across the genome has found patterns of apparently "global" epistasis, in which the fitness effect of a mutation varies systematically with the fitness of the genetic background on which it occurs (21–28). Typically, this manifests as either diminishing returns for beneficial mutations or increasing costs for deleterious mutations, with mutations having a less positive or more negative effect on fitter backgrounds. These consistent patterns of global epistasis may give rise to the dominant evolutionary trend of declining adaptability, and in contrast to the complexity of idiosyncratic interactions, they suggest that historical contingency could be less critical in constraining adaptive trajectories (29).

Despite their importance, these dual descriptions of epistasis have not been satisfactorily unified. In one view, global epistasis results from non-specific fitness-mediated interactions among mutations (24). Such interactions may for example emerge from the topology of metabolic networks, which generates overall patterns of diminishing returns and increasing costs that eclipse the specific details of idiosyncratic interactions (30). In contrast, other recent theoretical work has proposed an alternative view, hypothesizing that apparent fitness-mediated epistasis can instead emerge as the generic consequence of idiosyncratic interactions, provided they are sufficiently numerous and widespread (19, 20). These two models have substantially different implications for the structure of fitness landscapes, which in turn influence our expectations of the repeatability and predictability of evolution and of the effect of chance and contingency on adaptation at both the genotypic and phenotypic level. Thus, this dichotomy plays a central role in understanding of how epistasis affects evolutionary dynamics.

Thus far, however, empirical work has been unable to distinguish between these perspectives. The key difficulty is that testing these ideas requires both depth and breadth: we must analyze landscapes involving enough loci that we sample idiosyncratic interactions that can potentially give rise to overall fitness-mediated trends, and we must survey possible combinations of these mutations at sufficient depth to quantify the role of higher-order interactions (including potential "global" non-specific fitness-mediated interactions). Importantly, larger landscapes are also necessary to reduce the influence of measurement error on the inference of epistasis and analysis of fitness-correlated trends (see Supplementary Materials, section 6.3). Achieving this depth and breadth is technically challenging, because it requires us to synchronize many mutations across the genome.

Here, we overcome this challenge by developing a method that exploits Cre-Lox recombination to create a combinatorially expanding CRISPR guide-RNA (gRNA) array in *Saccharomyces cerevisiae*, which allows us to iteratively generate mutations at distant loci via a gene drive mechanism (Fig. 1A). Briefly, strains of opposite mating type containing inducible Cre recombinase and *SpCas9* genes are mutated at one of two loci (*A* or *B*), and DNA encoding guide-RNAs (gRNAs) specific to the wild-type alleles at these loci are integrated into their genomes (Fig. S1). After mating to produce a diploid heterozygous at *A*

and *B*, we induce a gene drive to make the loci homozygous. This begins with expressing Cas9 and generating gRNA-directed double-strand breaks at the wild-type *A* and *B* alleles. These breaks are then repaired by the mutated regions of homologous chromosomes, making the diploid homozygous at these loci with at least 95% efficiency. Simultaneously, we express Cre to induce recombination that brings gRNAs into physical proximity on the same chromosome by way of flanking Lox sites, in a strategy similar to that described previously (*31*) (Fig. 1B). We then sporulate diploids and select haploids bearing the linked gRNAs from both parents. In parallel, we carry out this process with "pseudo-WT" versions of these loci, which contain synonymous changes that abolish gRNA recognition, but lack the non-synonymous change of interest. This creates a set of four strains, with all possible genotypes at loci *A* and *B*. Concurrently, we create separate sets of four strains with all possible genotypes at other pairs of loci (e.g., *C* and *D*).

 By iterating this process, we can rapidly assemble an exponentially expanding, combinatorially complete genotype library. We mate separate sets of four genotypes bearing all combinations of mutations at two loci each in an all-against-all cross, drive their mutations, recombine their gRNAs, and sporulate to produce a 16-strain library bearing all 4-locus mutation combinations. Repeating these steps in a third cycle with two 4-locus libraries of opposite mating type yields a 256-strain 8-locus library, and a complete landscape of up to 16 mutations (2¹⁶ strains) can be constructed in just four cycles.

We sought to use this method to construct a complete fitness landscape that would shed light on the structure of epistasis: are fitness-correlated trends primarily the product of a global coupling of mutations via fitness, or do they emerge as the consequence of idiosyncratic epistasis? To do so, we surveyed studies of natural variation (e.g., (32–36)) and experimental evolution (e.g., (37–39)) to identify mutations potentially relevant to adaptation in the laboratory strain. We selected a set of mutations that sample a wide range of cellular functions, such as membrane stress response, mitochondrial stability, and nutrient sensing. Our goal in making this choice was to maximize fitness variance while minimizing pathway-specific idiosyncratic interactions. We note that alternative choices of mutations, particularly if they were focused on a specific protein or pathway (or limited to those that accumulated along the line of descent in a single lineage), might exhibit very different patterns of epistasis, which would be characteristic of the particular details of that specific protein or pathway (or that specific adaptive trajectory). However, our goal here is to analyze potentially global patterns of epistasis among mutations across the genome that are relevant to fitness in a variety of conditions and hence represent an overall fitness landscape for the laboratory strain.

We thus implemented our gene-drive system to construct a near-complete landscape spanning 10 missense mutations in 10 genes (including essential genes) on 8 chromosomes: *AKL1* (S176P), *BUL2* (L883F), *FAS1* (G588A), *MKT1* (D30G), *NCS2* (H71L), *PMA1* (S234C), *RHO5* (G10S), *RPII* (E102D), *SCH9* (P220S), and *WHI2* (L262S) (Fig. 1C, Table S1). We found that a landscape of about this size is required to distinguish the two models (see SI section 6.3). Immediately before the final mating cycle, all strains were transformed with a unique DNA barcode next to the *LYS2* locus to enable high-throughput, sequencing-based competitive fitness assays (Fig. S2, S3). All strains in each replicate haploid library were genotyped at all 10 loci to confirm presence of the desired alleles (this step also ensures presence in the diploid libraries). After excluding strains due to gene drive failure, 875 out of 1024 (85.4%) genotypes remained in at least one library (and 407 in both biological replicates). We also performed whole genome sequencing of 96 randomly selected strains to rule out pervasive aneuploidies or influential but spurious background mutations. One aneuploidy was identified, and 3 spurious background mutations were observed at >5% frequency. Subsequent analysis showed that these were unlikely to systematically influence our findings (Table S2, and SI section 5.1).

To obtain fitness landscapes, we conducted replicate bulk barcode-based fitness assays on both pooled haploid and homozygous diploid versions of the genotype library in 6 distinctly stressful media environments: YPD + 0.4% acetic acid, YPD + 6 mM guanidium chloride, YPD + 35 µM suloctidil, YPD @ 37°C, YPD + 0.8 M NaCl, and SD + 10 ng/mL 4NQO (Fig. 1D). For each of 7 days, pools were allowed 7 generations of growth, and aliquots were sampled and sequenced at the barcode locus at generations 7, 14, 28, 42, and 49. We estimated the relative fitness of each genotype from changes in barcode frequencies through time, achieving consistent measurements across technical and biological replicates (Fig. 1E,F, S4). From these data, we inferred the background-averaged additive and epistatic effects of each mutation and combination of mutations, respectively (using LASSO regularization, see

139 140 141

142 143

144

145

146

147

148 149

150

151

130

131 132

133 134

135

136 137

138

We found that our six environments yield substantially different landscapes, as demonstrated by the relatively low between-environment correlations of genotype fitnesses (Fig. 2A), the additive effects of each mutation (Fig. 2B), and the pairwise interactions between them (Fig. 2C). Haploid and homozygous diploid landscapes were largely correlated, but there were several notable exceptions, particularly in the suloctidil environment (Fig. 2A,B). And although some pairwise interactions remain roughly constant in strength, even as the corresponding additive effects vary considerably (e.g., RHO5 and WHI2), most wax and wane across environments (Fig. 2C). Nevertheless, the overall contribution from different epistatic orders shows some similarities across ploidies and environments (the magnitudes do differ; Fig. 2D), with additive and pairwise terms explaining most of the variance in the data, third-order terms contributing minorly, and the remaining orders making little difference, consistent with earlier studies (40). Across all epistatic orders, inferred effects were highly skewed, with a small number of terms explaining disproportionate variance (Fig. 2E).

152 153 154

155

156

157

158 159

160

161

We next sought to investigate potential patterns of global fitness-mediated epistasis. To do so, for each locus in each ploidy and environment, we plotted the fitness of a genotype with the mutated allele, φ_{Mut} , against the fitness of the same genotype with the WT allele, φ_{WT} . A regression slope, b, different from 1 in these plots signifies a fitness-correlated trend (FCT) (Fig. 3A, left; see SI). We note that some previous work has instead plotted the fitness effect of a mutation, $\Delta \varphi$, as a function of background fitness φ_{WT} . The advantage of our formulation here is that it does not privilege a specific allele as the "wild-type." Instead. regression in our plots translates intuitively when reversing direction to treat the reversion as the mutation: $b_{rev} = 1/b_{orig}$ by weighted-total least squares; see expanded discussion in the Supplementary Material, Fig. S5-S8.

162 163 164

165

166

167

We found that FCTs are common in our landscapes: across all ploidies, environments, and loci, ~44% of regression slopes deviate substantially from 1 (i.e., $b \le 0.9$ or $b \ge 0.9^{-1}$; these deviations are all significant; Fig. 3B, see histogram; Fig. S13 and S14). However, FCTs were not universal for fitness-affecting mutations: of the 49 examples across ploidies and environments of mutations with additive effects of magnitude > 0.5%, 18 were associated with $0.9 < b < 0.9^{-1}$ (Fig. 3B).

168 169 170

171

172

173

174

175 176

177

By partitioning background genotypes by the presence or absence of specific mutations, we can determine whether FCTs are truly "global" (i.e., they transcend these partitions and any corresponding idiosyncratic interactions; Fig. 3A, middle), or are instead fundamentally idiosyncratic (i.e., they emerge from regression across partitions shifted in ϕ_{Mut} versus ϕ_{WT} space by sparse interactions with specific background loci; Fig. 3A, right). When we partitioned FCTs by the presence or absence of interacting mutations in the background, we found several instances where the idiosyncratic model clearly explains the fitness-correlated trend. For example, the effect of the G10S mutation in RHO5 at 37°C exhibits a clear FCT (b = 0.76) (Fig. 3C). However, we can partition points by the presence of interacting WHI2 and AKL1 alleles in the background. Doing so shows that pairwise interactions with these alleles cause systematic shifts in φ_{10S} vs φ_{10G} space, with each partition assuming a slope near 1. Thus, over a range of

background fitnesses, a FCT in the effect of the G10S emerges from these specific idiosyncratic interactions (Fig. 3C, S11). In the case of the homozygous AKL1 S176P mutation in suloctidil, we observe a similar decomposition of a FCT (b = 1.29) when partitioning genotypes according to the presence of three interacting loci in the background (MKT1, RHO5, and WHI2) (Fig. 3D, S11). However, in other cases it is less clear whether the FCT can be partitioned in this way, and since deeper partitions tend to reduce background fitness variance and limit our confidence in regression slopes, a different approach is required to characterize the extent to which idiosyncratic terms cause FCTs across our data.

To investigate this question, we therefore analyzed the effect of removing specific idiosyncratic epistatic terms on the overall fitness-correlated trends. To do so, for each focal locus (in each ploidy and environment) we first calculated the weighted sum of squared errors (4I) of observed fitnesses from the global regression line (SSE $_{b=global}$) and from a fitted line of slope 1 (SSE $_{b=1}$, which corresponds to no FCT). We then set the largest epistatic term to zero and recalculated the expected fitness of each resulting genotype (assuming all other terms and residuals are non-zero), again obtaining both SSE $_{b=global}$ and SSE $_{b=1}$. If the fitness-correlated trend arose from a global effect, we expect that SSE $_{b=global}$ would be less than SSE $_{b=1}$ even as terms are removed. Instead, we found that, after removing the effect of just a few terms, a regression with a fixed slope of b=1 typically fit the data better than the b=global FCT slope (Fig. 3E, S11, with FCT threshold set to $b \le 0.9$ or 0.8)), approaching the fit of an unconstrained regression that minimizes SSE (i.e., the final slope approaches 1, Fig. S10). This indicates that the apparent FCT arises from these few idiosyncratic interactions, even for global slopes very different from 1. Although we also documented cases where b=global fit the data better than b=1 even after removing many terms, we expect most if not all these instances may be due to measurement error, since they tend to arise in ploidies and environments where the data is noisier (Fig. S17).

To further evaluate whether idiosyncratic interactions between these mutations are sufficient to generate FCTs, we performed the converse analysis, this time with genotype fitnesses as predicted by our model of additive and idiosyncratic epistatic terms. Instead of removing the effects of epistatic terms one at a time, we first stripped from the model all interactions involving the focal locus, yielding perfectly linear points of slope 1 when plotting φ_{Mut} vs φ_{WT} . We then added interactions one by one to our fitness prediction, from largest to smallest, and examined the resulting slopes. As shown in Fig. 3F for the haploid *PMA1* S234C mutation in 4NQO, adding just a handful of terms associated with 3 background loci recapitulates a strong FCT. Repeating this analysis with all our mutations shows that, on average, just 4 idiosyncratic interactions (primarily pairwise) are sufficient to recapitulate the full-model FCTs (a slope within 0.01 of the global slope, Fig. 3G, orange; see SM), which is far lower than the total number of inferred terms (median of 53) but represents on average 89% of the potential variance explained that could have been added (Fig. S12). Thus, although fitness-correlated trends are real and likely have important biological consequences, our data demonstrate that apparent fitness-mediated epistasis can readily emerge from remarkably few low-order idiosyncratic interactions.

Since the landscapes we study here have no natural polarization (i.e., neither allele is the assumed wildtype), we cannot comment directly on why earlier studies of global epistasis have more commonly found negative than positive FCTs (when plotting $\Delta \varphi$ versus φ_{WT}). However, this distribution of FCT directions is important because it may underly the ubiquitous trend of declining adaptability observed across laboratory evolution experiments (29). The observed bias towards negative trends may arise from asymmetries in the average sign of epistatic interactions between mutations away from extant high-fitness genotypes relative to their reversions, which theory has predicted should arise from idiosyncratic interactions (19, 20). In addition, we note that choosing polarizations at random will lead to more negative than positive FCTs across the full parameter space (see extended discussion in the SI).

Regardless of the cause of any asymmetry in the direction of fitness-correlated trends, our results support recent theoretical arguments that fitness-mediated epistasis can emerge as the generic consequence of widespread idiosyncratic interactions, rather than reflecting a global fitness-mediated coupling of mutations. Indeed, at least in our system, we see that fitness-correlated trends can arise even from a relatively small number of low-order interactions. We note that landscapes involving other types of variation (e.g., within a single protein or pathway or along the line of descent in a single lineage (21)) may exhibit different patterns, though we may expect these scenarios to involve an even stronger role for idiosyncratic interactions. More generally, we emphasize that idiosyncratic epistasis and global fitness-mediated effects are not mutually exclusive, and although fitness-correlated trends can be explained by the former in our system, in other cases both effects may contribute. However, our results suggest that nonspecific global epistasis may not be the primary driver of patterns of declining adaptability in laboratory evolution experiments, and this has general implications for the ways in which epistasis constrains evolutionary trajectories.

Acknowledgments: We thank the Bauer Core facility at Harvard, Gautam Reddy, Boris Shraiman, and members of the Desai lab for experimental assistance and comments on the manuscript. We thank Artur Rego-Costa for his help in creating Fig. 2C. Computational work was performed on the Odyssey cluster supported by the Research Computing Group at Harvard University.

245246247

248249

250

251

252

253254

255

244

242243

Funding:

Department of Defense (DoD), National Defense Science & Engineering Graduate (NDSEG) Fellowship Program (CWB)

Natural Sciences and Engineering Research Council of Canada, Postdoctoral fellowship,

Discovery Grant RGPIN-2021-02716, and Discovery Launch supplement DGECR-2021-00117 (ANNB)

National Human Genome Research Institute of the National Institutes of Health award F31-

HG010984 (YS)

National Science Foundation grant PHY-1914916 (MMD) National Institutes of Health grant GM104239 (MMD)

256257258

259

260

261

262

263

264

265266

267

Author contributions:

Conceptualization: ANNB, CWB, YS, JIR, MMD

Methodology: ANNB, CWB, YS, JIR

Investigation: CWB, ANNB Formal analysis: CWB, ANNB Visualization: CWB, ANNB Funding acquisition: MMD

Resources: MMD Supervision: MMD

Writing – original draft: CWB, ANNB, MMD Writing – review & editing: CWB, ANNB, MMD

268269270

Competing interests: Authors declare that they have no competing interests.

271272

Data and materials availability: Raw sequencing data are available at the NCBI Sequence Read Archive (accession no. PRJNA815849), and analysis code is available from Github (42). All other data described in the paper are presented in the main text or supplementary materials.

274275276

273

Supplementary Materials

- 277 Materials and Methods
- 278 Supplementary Text
- 279 Figs. S1 to S17
- Table S1
- 281 References (*43*–*59*)
- 282 Data S1 to S3

References and Notes

- D. J. Kvitek, G. Sherlock, Reciprocal sign epistasis between frequently experimentally evolved adaptive mutations causes a rugged fitness landscape. *PLoS Genet.* **7**, e1002056 (2011).
- 288 2. P. A. Romero, F. H. Arnold, Exploring protein fitness landscapes by directed evolution. *Nat Rev Mol Cell Biol.* **10**, 866–876 (2009).
- 3. K. M. Flynn, T. F. Cooper, F. B.-G. Moore, V. S. Cooper, The environment affects epistatic interactions to alter the topology of an empirical fitness landscape. *PLoS Genet.* **9**, e1003426 (2013).
- M. Costanzo, B. VanderSluis, E. N. Koch, A. Baryshnikova, C. Pons, G. Tan, W. Wang, M. Usaj, J.
 Hanchard, S. D. Lee, V. Pelechano, E. B. Styles, M. Billmann, J. van Leeuwen, N. van Dyk, Z.-Y.
- Lin, E. Kuzmin, J. Nelson, J. S. Piotrowski, T. Srikumar, S. Bahr, Y. Chen, R. Deshpande, C. F.
- Kurat, S. C. Li, Z. Li, M. M. Usaj, H. Okada, N. Pascoe, B.-J. San Luis, S. Sharifpoor, E. Shuteriqi,
- S. W. Simpkins, J. Snider, H. G. Suresh, Y. Tan, H. Zhu, N. Malod-Dognin, V. Janjic, N. Przulj, O.
- G. Troyanskaya, I. Stagljar, T. Xia, Y. Ohya, A.-C. Gingras, B. Raught, M. Boutros, L. M.
- Steinmetz, C. L. Moore, A. P. Rosebrock, A. A. Caudy, C. L. Myers, B. Andrews, C. Boone, A
- 299 global genetic interaction network maps a wiring diagram of cellular function. *Science*. **353** (2016),
- 300 doi:10.1126/science.aaf1420.
- 5. A. D. Norris, X. Gracida, J. A. Calarco, CRISPR-mediated genetic interaction profiling identifies RNA binding proteins controlling metazoan fitness. *Elife*. **6** (2017), doi:10.7554/eLife.28129.
- 303 6. M. A. Horlbeck, A. Xu, M. Wang, N. K. Bennett, C. Y. Park, D. Bogdanoff, B. Adamson, E. D. Chow, M. Kampmann, T. R. Peterson, K. Nakamura, M. A. Fischbach, J. S. Weissman, L. A.
- Gilbert, Mapping the Genetic Landscape of Human Cells. *Cell.* **174**, 953-967.e22 (2018).
- 306 7. K. S. Sarkisyan, D. A. Bolotin, M. V. Meer, D. R. Usmanova, A. S. Mishin, G. V. Sharonov, D. N.
- Ivankov, N. G. Bozhanova, M. S. Baranov, O. Soylemez, N. S. Bogatyreva, P. K. Vlasov, E. S.
- Egorov, M. D. Logacheva, A. S. Kondrashov, D. M. Chudakov, E. V. Putintseva, I. Z. Mamedov, D.
- S. Tawfik, K. A. Lukyanov, F. A. Kondrashov, Local fitness landscape of the green fluorescent
- protein. *Nature*. **533**, 397–401 (2016).
- 8. C. A. Olson, N. C. Wu, R. Sun, A comprehensive biophysical description of pairwise epistasis throughout an entire protein domain. *Curr Biol.* **24**, 2643–2651 (2014).
- 9. S. Bershtein, M. Segal, R. Bekerman, N. Tokuriki, D. S. Tawfik, Robustness-epistasis link shapes the fitness landscape of a randomly drifting protein. *Nature*. **444**, 929–932 (2006).
- 315 10. N. C. Wu, J. Otwinowski, A. J. Thompson, C. M. Nycholat, A. Nourmohammad, I. A. Wilson,
- Major antigenic site B of human influenza H3N2 viruses has an evolving local fitness landscape. *Nat*
- 317 *Commun.* **11**, 1233 (2020).
- 318 11. V. O. Pokusaeva, D. R. Usmanova, E. V. Putintseva, L. Espinar, K. S. Sarkisyan, A. S. Mishin, N. S.
- Bogatyreva, D. N. Ivankov, A. V. Akopyan, S. Y. Avvakumov, I. S. Povolotskaya, G. J. Filion, L. B.
- 320 Carey, F. A. Kondrashov, An experimental assay of the interactions of amino acids from orthologous
- sequences shaping a complex fitness landscape. *PLoS Genet.* **15**, e1008079 (2019).

- 12. J. I. Jiménez, R. Xulvi-Brunet, G. W. Campbell, R. Turk-MacLeod, I. A. Chen, Comprehensive 322
- 323 experimental fitness landscape and evolutionary network for small RNA. Proc Natl Acad Sci USA.
- 324 **110**, 14984–14989 (2013).
- 13. B. Madan, B. Zhang, K. Xu, C. W. Chao, S. O'Dell, J. R. Wolfe, G.-Y. Chuang, A. S. Fahad, H. 325
- Geng, R. Kong, M. K. Louder, T. D. Nguyen, R. Rawi, A. Schön, Z. Sheng, R. Nimrania, Y. Wang, 326
- T. Zhou, B. C. Lin, N. A. Doria-Rose, L. Shapiro, P. D. Kwong, B. J. DeKosky, Mutational fitness 327
- landscapes reveal genetic and structural improvement pathways for a vaccine-elicited HIV-1 broadly 328
- neutralizing antibody. Proc Natl Acad Sci U S A. 118 (2021), doi:10.1073/pnas.2011653118. 329
- 330 14. N. C. Wu, L. Dai, C. A. Olson, J. O. Lloyd-Smith, R. Sun, Adaptation in protein fitness landscapes is facilitated by indirect paths. *Elife*. **5** (2016), doi:10.7554/eLife.16965. 331
- 15. C. Bank, S. Matuszewski, R. T. Hietpas, J. D. Jensen, On the (un)predictability of a large intragenic 332 fitness landscape. Proc Natl Acad Sci USA. 113, 14085–14090 (2016). 333
- 16. J. Domingo, G. Diss, B. Lehner, Pairwise and higher-order genetic interactions during the evolution 334 335 of a tRNA. Nature. 558, 117–121 (2018).
- 17. J. Teyra, A. Ernst, A. Singer, F. Sicheri, S. S. Sidhu, Comprehensive analysis of all evolutionary 336 paths between two divergent PDZ domain specificities. *Protein Sci.* **29**, 433–442 (2020). 337
- 18. T.-L. V. Lite, R. A. Grant, I. Nocedal, M. L. Littlehale, M. S. Guo, M. T. Laub, Uncovering the basis 338 339 of protein-protein interaction specificity with a combinatorially complete library. Elife. 9 (2020),
- doi:10.7554/eLife.60924. 340
- 19. D. M. Lyons, Z. Zou, H. Xu, J. Zhang, Idiosyncratic epistasis creates universals in mutational effects 341 342 and evolutionary trajectories. *Nat Ecol Evol.* **4**, 1685–1693 (2020).
- 20. G. Reddy, M. M. Desai, Global epistasis emerges from a generic model of a complex trait. *Elife*. 10 343 (2021), doi:10.7554/eLife.64740. 344
- 21. A. I. Khan, D. M. Dinh, D. Schneider, R. E. Lenski, T. F. Cooper, Negative epistasis between 345 beneficial mutations in an evolving bacterial population. Science. 332, 1193–1196 (2011). 346
- 22. H.-H. Chou, H.-C. Chiu, N. F. Delaney, D. Segrè, C. J. Marx, Diminishing returns epistasis among 347 beneficial mutations decelerates adaptation. Science. 332, 1190–1192 (2011). 348
- 23. L. Perfeito, A. Sousa, T. Bataillon, I. Gordo, Rates of fitness decline and rebound suggest pervasive 349 epistasis. Evolution. 68, 150–162 (2014). 350
- 24. S. Kryazhimskiy, D. P. Rice, E. R. Jerison, M. M. Desai, Microbial evolution, Global epistasis 351 352 makes adaptation predictable despite sequence-level stochasticity. Science. 344, 1519–1522 (2014).
- 353 25. M. S. Johnson, A. Martsul, S. Kryazhimskiy, M. M. Desai, Higher-fitness yeast genotypes are less robust to deleterious mutations. Science. 366, 490–493 (2019). 354
- 355 26. X. Wei, J. Zhang, Patterns and Mechanisms of Diminishing Returns from Beneficial Mutations. *Mol* Biol Evol. 36, 1008–1021 (2019). 356

- 357 27. S. Schoustra, S. Hwang, J. Krug, J. A. G. M. de Visser, Diminishing-returns epistasis among random
- beneficial mutations in a multicellular fungus. *Proc Biol Sci.* **283** (2016),
- doi:10.1098/rspb.2016.1376.
- 360 28. R. C. MacLean, G. G. Perron, A. Gardner, Diminishing returns from beneficial mutations and
- pervasive epistasis shape the fitness landscape for rifampicin resistance in Pseudomonas aeruginosa.
- 362 *Genetics*. **186**, 1345–1354 (2010).
- 363 29. A. Couce, O. A. Tenaillon, The rule of declining adaptability in microbial evolution experiments.
- 364 Front Genet. **6**, 99 (2015).
- 365 30. S. Kryazhimskiy, Emergence and propagation of epistasis in metabolic networks. *Elife.* **10** (2021),
- doi:10.7554/eLife.60200.
- 31. A. N. Nguyen Ba, I. Cvijović, J. I. Rojas Echenique, K. R. Lawrence, A. Rego-Costa, X. Liu, S. F.
- Levy, M. M. Desai, High-resolution lineage tracking reveals travelling wave of adaptation in
- laboratory yeast. *Nature*. **575**, 494–499 (2019).
- 32. H. Sinha, L. David, R. C. Pascon, S. Clauder-Münster, S. Krishnakumar, M. Nguyen, G. Shi, J.
- Dean, R. W. Davis, P. J. Oefner, J. H. McCusker, L. M. Steinmetz, Sequential elimination of major-
- effect contributors identifies additional quantitative trait loci conditioning high-temperature growth
- in yeast. *Genetics*. **180**, 1661–1670 (2008).
- 33. S. W. Doniger, H. S. Kim, D. Swain, D. Corcuera, M. Williams, S.-P. Yang, J. C. Fay, A catalog of
- neutral and deleterious polymorphism in yeast. *PLoS Genet.* **4**, e1000183 (2008).
- 376 34. E. X. Kwan, E. Foss, L. Kruglyak, A. Bedalov, Natural polymorphism in BUL2 links cellular amino
- acid availability with chronological aging and telomere maintenance in yeast. *PLoS Genet.* 7,
- 378 e1002250 (2011).
- 35. J. S. Bloom, I. M. Ehrenreich, W. T. Loo, T.-L. V. Lite, L. Kruglyak, Finding the sources of missing
- heritability in a yeast cross. *Nature*. **494**, 234–237 (2013).
- 36. D. M. Wloch-Salamon, K. Tomala, D. Aggeli, B. Dunn, Adaptive Roles of SSY1 and SIR3 During
- 382 Cycles of Growth and Starvation in Saccharomyces cerevisiae Populations Enriched for Quiescent or
- Nonquiescent Cells. *G3 (Bethesda)*. 7, 1899–1911 (2017).
- 37. B. Szamecz, G. Boross, D. Kalapis, K. Kovács, G. Fekete, Z. Farkas, V. Lázár, M. Hrtyan, P.
- Kemmeren, M. J. A. Groot Koerkamp, E. Rutkai, F. C. P. Holstege, B. Papp, C. Pál, The genomic
- landscape of compensatory evolution. *PLoS Biol.* **12**, e1001935 (2014).
- 38. L. M. Kohn, J. B. Anderson, The underlying structure of adaptation under strong selection in 12
- experimental yeast populations. *Eukaryot Cell.* **13**, 1200–1206 (2014).
- 39. S. Venkataram, B. Dunn, Y. Li, A. Agarwala, J. Chang, E. R. Ebel, K. Geiler-Samerotte, L.
- Hérissant, J. R. Blundell, S. F. Levy, D. S. Fisher, G. Sherlock, D. A. Petrov, Development of a
- Comprehensive Genotype-to-Fitness Map of Adaptation-Driving Mutations in Yeast. *Cell.* **166**,
- 392 1585-1596.e22 (2016).
- 40. D. M. Weinreich, Y. Lan, J. Jaffe, R. B. Heckendorn, The Influence of Higher-Order Epistasis on
- Biological Fitness Landscape Topography. J Stat Phys. 172, 208–225 (2018).

395 41. D. York, N. M. Evensen, M. L. Martínez, J. De Basabe Delgado, Unified equations for the slope, intercept, and standard errors of the best straight line. *American Journal of Physics.* **72**, 367–375

397 (2004).

- 398 42. C. W. Bakerlee, A. N. Nguyen Ba, *Fitness-correlated trends analysis pipeline publication archive* (Zenodo, 2022; https://zenodo.org/record/6352707).
- 43. C. B. Brachmann, A. Davies, G. J. Cost, E. Caputo, J. Li, P. Hieter, J. D. Boeke, Designer deletion strains derived from Saccharomyces cerevisiae S288C: a useful set of strains and plasmids for PCRmediated gene disruption and other applications. *Yeast.* 14, 115–132 (1998).
- 403 44. R. D. Gietz, Yeast transformation by the LiAc/SS carrier DNA/PEG method. *Methods Mol Biol.* 404 1205, 1–12 (2014).
- 405 45. A. M. Deutschbauer, R. W. Davis, Quantitative trait loci mapped to single-nucleotide resolution in yeast. *Nat. Genet.* **37**, 1333–1340 (2005).
- 46. F. Storici, L. K. Lewis, M. A. Resnick, In vivo site-directed mutagenesis using oligonucleotides.
 Nat. Biotechnol. 19, 773–776 (2001).
- 47. A. H. Y. Tong, C. Boone, in *Yeast Protocol*, W. Xiao, Ed. (Humana Press, 2006;
 410 http://link.springer.com.myaccess.library.utoronto.ca/protocol/10.1385/1-59259-958-3%3A171),
 411 *Methods in Molecular Biology*, pp. 171–191.
- 48. D. S. M. Ottoz, F. Rudolf, J. Stelling, Inducible, tightly regulated and growth condition-independent transcription factor in Saccharomyces cerevisiae. *Nucleic Acids Res.* **42**, e130 (2014).
- 49. J. E. DiCarlo, J. E. Norville, P. Mali, X. Rios, J. Aach, G. M. Church, Genome engineering in Saccharomyces cerevisiae using CRISPR-Cas systems. *Nucleic Acids Res.* **41**, 4336–4343 (2013).
- M. Plass, Yeast Intron Structures Database, (available at http://regulatorygenomics.upf.edu/Software/Yeast_Introns/documentation.html).
- 51. C. Engler, R. Kandzia, S. Marillonnet, A one pot, one step, precision cloning method with high throughput capability. *PLoS ONE*. **3**, e3647 (2008).
- 52. C. Engler, R. Gruetzner, R. Kandzia, S. Marillonnet, Golden gate shuffling: a one-pot DNA shuffling method based on type IIs restriction enzymes. *PLoS ONE*. 4, e5553 (2009).
- 422 53. M. Baym, S. Kryazhimskiy, T. D. Lieberman, H. Chung, M. M. Desai, R. Kishony, Inexpensive multiplexed library preparation for megabase-sized genomes. *PLoS ONE*. **10**, e0128036 (2015).
- 54. D. E. Deatherage, J. E. Barrick, Identification of mutations in laboratory-evolved microbes from next-generation sequencing data using breseq. *Methods Mol Biol.* **1151**, 165–188 (2014).
- 426 55. M. Barnett, *regex: Alternative regular expression module, to replace re.* 427 (https://bitbucket.org/mrabarnett/mrab-regex).
- 428 56. A. N. Nguyen Ba, K. R. Lawrence, A. Rego-Costa, S. Gopalakrishnan, D. Temko, F. Michor, M. M.
- Desai, Barcoded Bulk QTL mapping reveals highly polygenic and epistatic architecture of complex
- traits in yeast. *Elife*. **11**, e73983 (2022).

- 431 57. P. Zhao, B. Yu, On Model Selection Consistency of Lasso. *Journal of Machine Learning Research*.
 432 7, 2541–2563 (2006).
- 433 58. J. Yang, S. H. Lee, M. E. Goddard, P. M. Visscher, GCTA: a tool for genome-wide complex trait analysis. *Am. J. Hum. Genet.* **88**, 76–82 (2011).
- 59. D. Berger, E. Postma, Biased estimates of diminishing-returns epistasis? Empirical evidence revisited. *Genetics*. **198**, 1417–1420 (2014).

Figure Captions

439 440 441

442

443

444

445 446

447

448 449

450

451 452

453

454 455

Fig. 1. Recombining CRISPR-gene drive system. (A) Experimental design. Strains of opposite mating type carrying known mutations and corresponding guide-RNAs (gRNAs) mate to form heterozygous diploids. Cas9 expression "drives" these mutations, and site-specific recombination links gRNAs. Homozygous diploids are sporulated, haploids with linked gRNAs are selected, and the process repeats, incorporating exponentially increasing numbers of mutations. (B) Recombining gene drive system. gRNAs targeting heterozygotic loci are flanked by selection markers and two of three orthogonal Lox sites (colored triangles), which are inactivated through recombination (red triangles). Cas9 "drives" targeted mutations, whereas Cre-Lox recombination brings like markers to the same chromosome and activates a URA3 gene interrupted by an artificial intron. Following sporulation, the chromosome with gRNAs is selected using the markers of interest whereas the other is counterselected using 5-FOA. (C) Cross design. A complete fitness landscape is produced in parallel by distinct cross designs that yield final homozygous diploids and haploids in biological replicates with unique DNA barcodes. (D) Bulk-fitness assays. Pooled strains are assayed in replicate for competitive fitness in several environments by sequencing barcodes to obtain strain frequencies over time. (E) Repeatability of technical replicate competitive fitness measurements. (F) Repeatability of biological replicate competitive fitness measurements.

456 457 458

459

460

461

462

463

464 465 **Fig. 2. Fitness landscapes. (A)** Correlation in observed fitness (upper right) and predicted fitness (from inferred model, lower left, see SI section 5.1) across ploidies and environments. (**B**) Background-averaged additive effect of each locus across ploidies and environments. Error bars represent 95% confidence intervals. (**C**) Background-averaged pairwise epistatic effects between loci across ploidies and environments. Weights of edges connecting loci represent the proportion of pairwise variance explained by each interaction. Heights of bars on the perimeter correspond to the proportion of additive variance explained by each locus in each environment. (**D**) Variance partitioning of broad-sense heritability from additive and epistatic orders across ploidies and environments. (**E**) Cumulative distribution of the epistatic variance explained by rank-ordered epistatic terms of all orders.

466 467

468

469

470

471

472

473 474

475

476

477

478

479

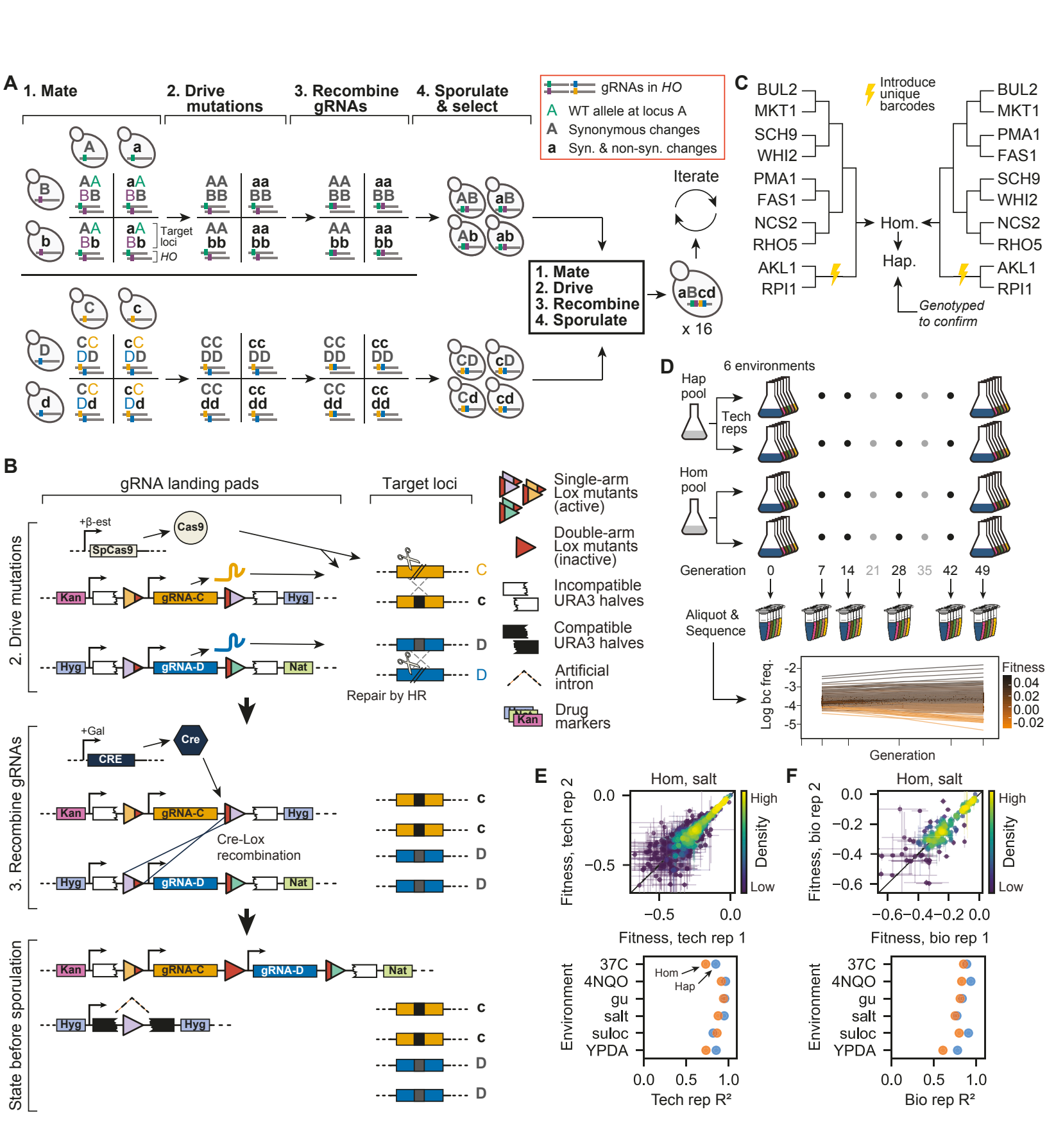
480 481

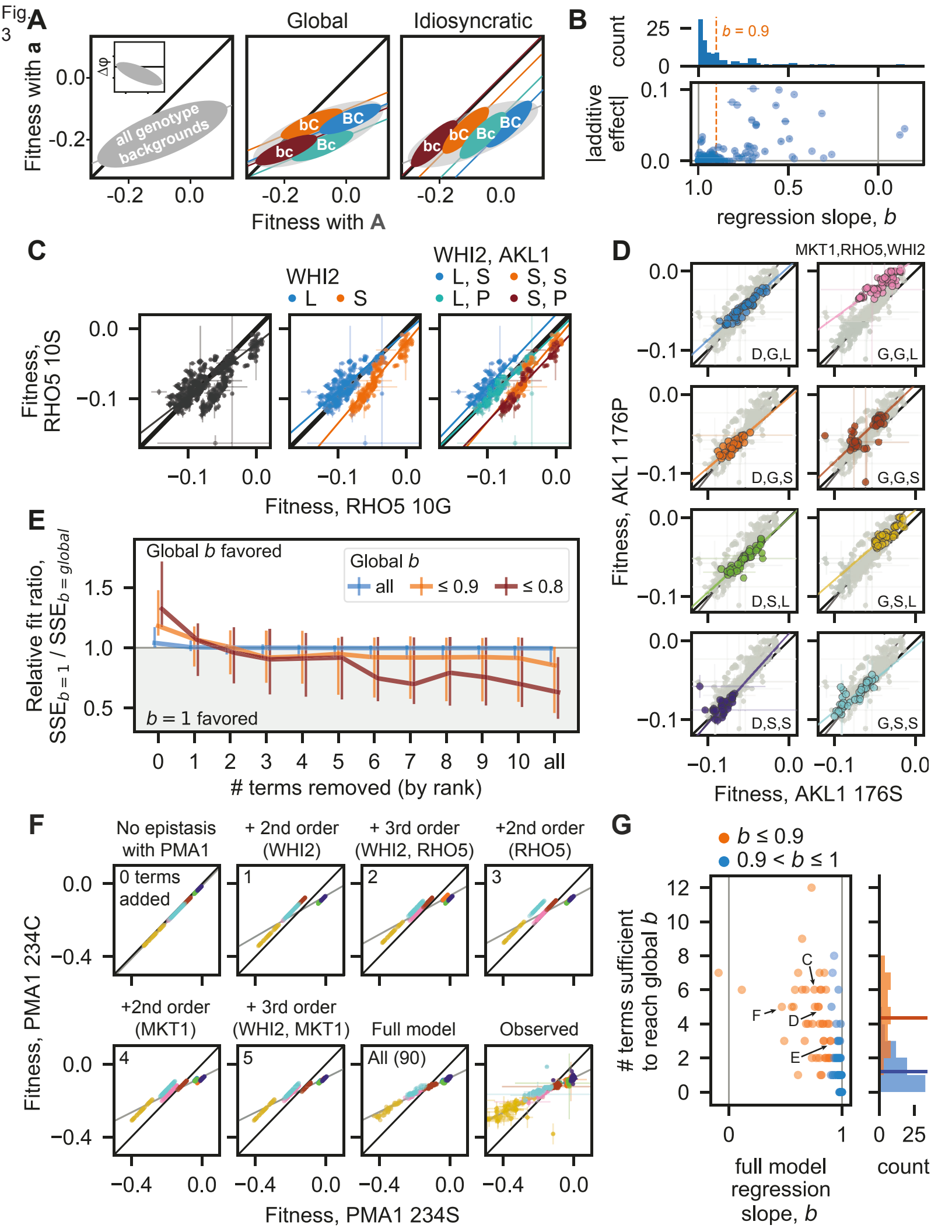
482

483

484 485

Fig. 3. Fitness-correlated trends (FCTs). (A) Schematic contrasting how global or idiosyncratic epistasis could produce FCTs. Inset shows FCT analyzed as the effect of a mutation ($\Delta \varphi$) on backgrounds of different fitnesses. (B) Histogram and scatterplot of regression slopes, b, between φ_{Mut} and φ_{WT} and corresponding absolute additive effects of mutations. Polarity adopted such that $b \le 1$. Total error bar length is twice the standard error of the slope. (C) Fitness effect of *RHO5* mutation (G10S) (φ_{Mut} versus φ_{WT}) in all haploid backgrounds at 37°C (left) and partitioned by genotypes at WHI2 (L262S) (middle) and WHI2 and AKLI (S176P) (right). Initial $SSE_{b=1} / SSE_{b=global}$ is 1.21. (D) Fitness effect of AKLI mutation in all homozygote backgrounds in the suloctidil environment, partitioned by genotypes at MKT1 (D30G), RHO5, and WHI2. Initial $SSE_{b=1} / SSE_{b=global}$ is 1.31. (E) Median relative fit ratio between regressions with fixed slope of b=1 and b=global, as function of number of epistatic terms removed from observed phenotypes. Vertical lines represent interquartile range. Polarity adopted such that $b \le 1$. (F) Inferred fitness effect of *PMA1* S234C mutation in 4NQO environment across all haploid backgrounds. Epistatic terms interacting with *PMA1* are completely removed from genotype fitnesses, then added back sequentially (from largest to smallest). Bottom-right: full-model (inferred) and observed genotype fitnesses, respectively. Grey line is regression slope. (G) Scatterplot and histograms of FCT regression slopes for all data, and number of epistatic terms sufficient to recapitulate them. Horizontal lines in histogram indicate means. Arrows, letters indicate populations presented in previous panels. Polarity adopted such that $b \le 1$.





Supplementary Information

Contents

T		sign and construction of the combinatorial CRISPR gene-drive system and	
	libr	·	3
	1.1	Strains	3
	1.2	Mutations and their selection	3
	1.3	Construction of guide crRNA plasmids	4
	1.4	Final barcoding procedure	5
	1.5	Hierarchical mating procedure	6
2	Ger	notype verification	8
	2.1	Whole-genome sequencing	8
	2.2	Locus-specific multiplex PCR	9
	2.3	Counting alleles for each locus in each well	9
	2.4	Statistical inference of gene-drive failures	10
	2.5	Other genotyping	11
3	Cor	nbinatorial indexing and sequencing of barcodes	12
	3.1	Combinatorial pooling and sequencing	12
	3.2	Barcode assignment to single wells	
4	Bul	k phenotyping	13
	4.1	Growth experiments	13
	4.2	Amplicon barcode sequencing	13
	4.3	Fitness inference for time-dependent barcode frequencies	14
	4.4	Comparison between technical, biological replicates	
5	Qua	antitative analysis of epistasis	17
	5.1	Estimation of parameters	17
	5.2	Variance partitioning	18
6	Ana	alysis of fitness-correlated trends	18
	6.1	Fitting regression slopes to determine fitness-correlated trends	19
	6.2	Decomposition of fitness-correlated trends	23
	6.3	Quantifying the effect of landscape size in the analysis of fitness-correlated trends	27
7	Car	otions for Data Tables	32
	7.1	Data Table S1	32
	7.2	Data Table S2	
	7 3	Data Table S3	39

List of Figures

	S1	gRNA integration plasmids	5
	S2	Barcoding plasmid	6
	S3		8
	S4	Comparison of technical and biological replicates for all ploidies and assay environments	16
	S5	Slopes and their reversions in the $\Delta \phi$ formulation	20
	S6	Comparison of fitness correlated trends for a simple case	21
	S7	Comparison of fitness correlated trends for a complicated case	22
	S8	Comparison of fitness correlated trends for a case where the orientation matters	22
	S9	Effect of parameters on global regression in the ϕ_{wt}/ϕ_{mut} formulation	24
	S10	Absolute fit comparison in term removal analysis	25
	S11	Relative fit ratios for each locus	26
	S12	Terms, epistasis sufficient to recapitulate global slopes	27
	S13	Scatterplots of ϕ_{wt}/ϕ_{mut} for all loci in haploid form	28
	S14	Scatterplots of ϕ_{wt}/ϕ_{mut} for all loci in homozygous form	29
	S15	FCT resolved as idiosyncratic in nature with respect to landscape size in 4NQO	
		(haploid)	31
	S16	FCT resolved as idiosyncratic in nature with respect to landscape size at 37C (haploid)	31
	S17	Final relative fit ratio as a function of reproducibility in biological replicates	32
Li	st o	f Tables	
	S1	Mutations constructed in the experiment	4

Design and construction of the combinatorial CRISPR gene-drive system and library

3 1.1 Strains

The two parental strains used in this study, YAN548 and YAN564, differ at their mating type and are derived from the BY4742 [43] (S288C: MATa, his3 Δ 1, ura3 Δ 0, leu2 Δ 0, lys2 Δ 0) with several modifications required for our combinatorial CRISPR gene-drive strategy. We chose to work in this background due to its history in studies of epistasis in yeast [4] and ease of transformation [44].

S288C is a poor sporulator [45], and we introduced the RME1 promoter allele known to increase sporulation efficiency (ins-108A) in BY4742, creating YAN404. YAN407 was generated from YAN404 by mating-type switching using a centromeric plasmid carrying the HO endonuclease (pAN216a_pGAL1-HO_pSTE2-HIS3_pSTE3_LEU2). We then introduced the Cre recombinase under the control of the galactose promoter at the YBR209W locus using Delitto Perfetto [46], yielding YAN525 and YAN526. The CAN1 gene was subsequently replaced with a mating type reporter construct [47] (pSTE2-SpHIS5-pSTE3-LEU2) which expresses the HIS5 gene from $Schizosaccharomyces\ pombe$ (orthologous to the $S.\ cerevisiae\ HIS3$) in MATa cells, and the LEU2 gene in MAT α cells.

Cas9 was introduced close to the HO locus under the control of an estradiol-inducible promoter [48] (HO::SpCas9-B112-ER), generating the final strains YAN548 and YAN564. Preliminary work has shown that $2 \mu M \beta$ -estradiol is sufficient for robust Cas9 induction.

Starting strains containing specific mutations were constructed using dsDNA oligo-mediated repair using Cas9-mediated double-strand break. To do so, we created a centromeric plasmid carrying the URA3 gene that expressed the guide-RNA. Yeast cells were grown with β -estradiol to induce Cas9, and transformed at log-phase with the guide-RNA expressing plasmid and a double-stranded DNA oligonucleotide with the desired mutation. Cells were then recovered on SD-URA with β -estradiol to maintain expression of Cas9 and the guide-RNA. A parallel transformation can be done to assess the targetting efficiency as an efficient guide-RNA usually leads to far fewer surviving colonies during the transformation due to the toxicity of unrepaired Cas9-mediated double-strand break. Large colonies from the transformation were then grown in YPD overnight and spread on media containing 5-FOA (1 g/L) to counterselect the plasmid expressing the guide-RNA. All strains were then verified by Sanger sequencing.

1.2 Mutations and their selection

Mutations for our combinatorially-complete fitness landscape were chosen based on several factors. First, we used prior information from published and unpublished experiments that suggested fitness effects for our mutations in at least one environment. Second, due to the need to minimize guide-RNA recognition after the desired mutation is made, we focused on amino acid changes because synonymous mutations could also be incorporated. Third, mutations were chosen that would target a variety of cellular processes to maximize our ability to detect global epistasis. Finally, mutations were chosen that could be efficiently made and not negatively impact our CRISPR-Cas9 system described here (i.e., mutations should not make strains sterile, impair sporulation, or impact galactose metabolism).

Mutation	Sequence Information	Reference

WHI2 L262S	Guide RNA: ATGGATATGTTGTGCTCCTC	[37]
Chr XV	L262S DNA: GAcATGagtTGtTCCTCCGGA	
	L262L DNA: GAcATGcTaTGtTCCTCCGGA	
PMA1 S234C	Guide RNA: TGCTATTACTGGTGAATCTT	[38]
Chr VII	S234C DNA: ACTGGTGAATgccTtGCTGTC	
Essential gene	S234S DNA: ACTGGTGAATCccTtGCTGTC	
MKT1 D30G	Guide RNA: ATGGTTGACGTCTATATCCA	[35]
Chr XIV	D30G DNA: ACCCTGGgaATtGAtGTtAAC	
	D30D DNA: ACCCTGGAcATtGAtGTtAAC	
RHO5 G10S	Guide RNA: ATAATTGGTGATGGTGCAGT	Our lab
Chr XIV	G10S DNA: ATatcaGAcGGaGCAGTAGGT	
	G10G DNA: ATaGGaGAcGGaGCAGTAGGT	
AKL1 S176P	Guide RNA: TCGCGATGGATCAAGGACAC	[33]
Chr II	S176P DNA: CCTGTGcCtcTaATtCAcaGa	
	S176S DNA: CCTGTGTCtcTaATtCAcaGa	
BUL2 L883F	Guide RNA: CACAAACACGTTTCAAGATT	[34]
Chr XIII	L883F DNA: TGCCCAATtTcGAgACtTGT	
	L883L DNA: TGCCCAATtTgGAgACtTGT	
FAS1 G588A	Guide RNA: AATCGGTAGACCACCTTTAT	[36]
Chr XI	G588A DNA: ATCGcacGtCCtCCaTTATT	
Essential gene	G588G DNA: ATCGGacGtCCtCCaTTATT	
NCS2 H71L	Guide RNA: CTGAATCAGAATGTGATAAG	[32]
Chr XIV	H71L DNA: CTCCCCTTgagtttgagtGA	
	H71H DNA: CTCCCCTTgagtCAcagtGA	
SCH9 P220S	Guide RNA: TCTAATGGTCCTGAGTCACT	[39]
Chr VIII	P220S DNA: AAcGGatCaGAaTCACTAGGC	
	P220P DNA: AAcGGaCCaGAaTCACTAGGC	
RPI1 E102D	Guide RNA: GTAATGAATGCTATATCCTC	Our lab
Chr IX	E102D DNA: GAGCCTGAcGAcATtGCtTTC	
	E102E DNA: GAGCCTGAaGAcATtGCtTTC	
		

Table S1: Mutations constructed in the experiment. Lower case letters represent mutated sequences with respect to the wild-type DNA.

1.3 Construction of guide crRNA plasmids

Our combinatorial CRISPR gene-drive system allows a hierarchical construction of guide crRNA 42 arrays into a benign locus, by taking advantage of Cre-Lox recombination. Previously, we identified 43 three orthogonal and unidirectional recombination sites that are necessary for our design. Briefly, 44 our gene-drive system makes use of three types of recombining plasmids with three distinct pairs of 45 drug markers, which we refer to as type HygMX-KanMX, KanMX-NatMX, and NatMX-HygMX. The three drug markers - HygMX, KanMX, and NatMX - are resistance cassettes for hygromycin 47 B, G418, and nourseothricin, respectively, and differ additionally by the use of paralogous TEF 48 promoters and synthetic terminators as in [31]. Each type is based on an HO-targeting plasmid pAN3H0a (Figure S1), which contains the two drug marker cassettes for selection as well as homologous sequences that lead to integration of insert sequences with high efficiency. The insert

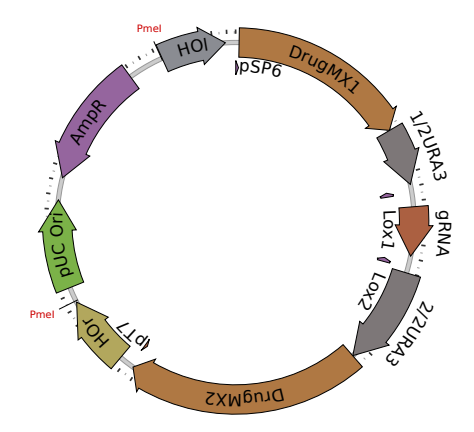


Figure S1: gRNA integration plasmids. We use three integration plasmids with different drug markers, Lox sites, and URA3 frameshift configurations as explained in Section 1.3.

sequences between the two drug cassettes contain one of 10 guide-RNA cassettes (each with an SNR52 promoter mutated at non-functional regions to reduce the rate of unintended homologous recombination, the guide-RNA, the structural RNA element and the SUP4 terminator [49]). In addition, each drug marker is linked to their own half of URA3 (frameshifted for each drug such that the first half of URA3 only functions properly when the correctly framed second half of URA3 is used) which contains a splice donor or acceptor (from QCR10 [50]) and their own orthogonal Lox site (LoxP, Lox2272, or Lox5171, with arm mutations to allow only a single recombination event between them [31]). In the configuration found at integration, the URA3 is not functional. However, when recombined properly by Cre recombinase, a configuration which brings like drug markers on the same chromosome (HygMX-HygMX, for example) will produce a functional URA3, which we can select with media lacking uracil and counterselect with media containing 5-FOA.

This system allows diploids created by mating two strains with compatible marker configurations to be selected on media containing all three drugs (described later in section Section 1.5). Compatible configurations will always include a common drug that will yield a functional URA3 after recombination. For example, the HygMX-KanMX configuration is compatible with KanMX-NatMX (which will form HygMX-NatMX and KanMX-KanMX after recombination) or with NatMX-HygMX (which will form NatMX-KanMX and HygMX-HygMX after recombination). The recombined 'landing pads' are thus compatible with each other (for example, HygMX-NatMX is compatible with NatMX-KanMX, which when recombined will form HygMX-KanMX and NatMX-NatMX).

1.4 Final barcoding procedure

To allow bulk phenotyping of the strains, we introduced a 22mer DNA barcode (16 random nucleotides and 6 known spacer nucleotides) alongside a complete LYS2 ORF at the LYS2 locus via homologous recombination in the AKL1-RPI1 double-mutant strains prior to the final mating step. To produce a library of uniquely barcoded plasmids, we generated an entry vector with 702 bp homologous region upstream of the LYS2 deletion, the deleted 293 bp region immediately upstream of the ORF, the 4179 bp LYS2 ORF, and then a 39 bp tGuo1 synthetic terminator. Downstream of this terminator was a primer-binding site, pBC1, followed by the ccdB gene, which is toxic in

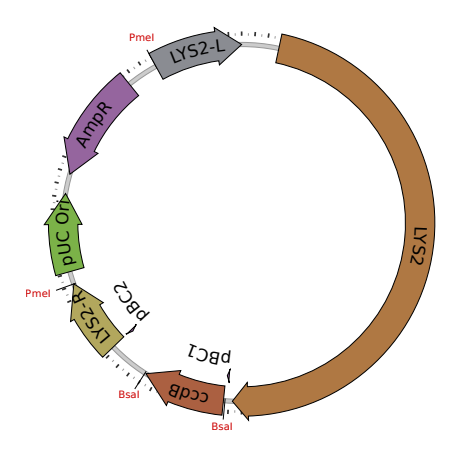


Figure S2: Barcoding plasmid before barcode insertion. We integrate a random barcode at the LYS2 locus to uniquely tag each individual in the pool.

E. coli strain DH10B. This gene was followed by 300 bp of semi-random DNA sequence (used as "filler" for obtaining PCR bands distinct from primer dimer bands), the pBC2 primer-binding site, and 589bp homologous to the region immediately downstream of the LYS2 deletion. Barcodes were cloned into this plasmid at the ccdB locus via Golden Gate assembly [51, 52] in 8 independent replicates, separately cloning in DH10B via electroporation and selecting on LB+Ampicillin sodium salt (100 μg/mL) agar plates (1% tryptone, 0.5% yeast extract, 0.5% sodium chloride, 1.5% agar) after an hour of recovery in SOC media (2% tryptone, 0.5% yeast extract, 8.56mM sodium chloride, 2.5mM potassium chloride, 10mM magnesium chloride, 10mM magnesium sulfate, 20mM glucose). Plates, which bore at least 30,000-40,000 transformant colonies each, were each scraped and cultured in 5mL LB+Amp media prior to miniprepping to isolate plasmid.

To barcode AKL1-RPI1 double mutants, we first isolated 10 individual colonies of each of the 4 possible double-mutant genotypes. We split these 10 colonies into two sets of 5. Each set of 5 colonies was cultured, pooled, and transformed with one of the eight barcode plasmid libraries, which had previously been cut with PmeI to linearize the region for integration. Transformants were selected on SD-Lys agar plates and, to the best of our abilities, individually picked into SD-Lys media for continued purifying growth.

1.5 Hierarchical mating procedure

The basic procedure for a cycle of mating, drive, recombination, and sporulation is as follows:

Strains with compatible guide-RNA "landing pads" and opposite mating type were mixed to generate diploids in YPD plus ampicillin ($100\,\mu\text{g/mL}$) via mating for 12-24 hours. Cells were then passaged to YPG (1% yeast extract, 2% peptone, 2% galactose) plus ampicillin liquid media containing hygromycin B (at $300\,\mu\text{g/mL}$), geneticin (at $200\,\mu\text{g/mL}$), and nourseothricin (at $100\,\mu\text{g/mL}$) to select for diploids, with selection sustained for at least 3 generations. Cells were then transferred to YPG containing all four drugs and at least $2\,\mu\text{M}$ β -Estradiol to induce Cre-recombinase and Cas9, with selection for at least 10 generations. This generates homozygous diploids at the loci targetted by Cas9, and combines the guide-RNA from the homologous HO loci onto the same chromosome. The cells were then grown in SD-Ura with β -estradiol for at least 15 generations to select for successful Cre-Lox recombinants. They then were induced to sporulate by 16-24 h growth

in YPA (1% yeast extract, 2% peptone, 1% potassium acetate) followed by culture in SPO media (1% potassium acetate, 0.005% zinc acetate). After 3-5 days of sporulation, haploids containing all the mutated loci and recombined gRNA loci were selected with at least 15 generations of growth in S/MSG-D (1.67% yeast nitrogen base lacking ammonium sulfate, 1% monosodium glutamate, 2% dextrose) lacking histidine or leucine (selecting for MATa and MAT α respectively), containing two of the three antibiotic drugs (depending on the landing pad configuration) and 1g/L 5-FOA to counterselect diploids. Finally, selected populations were screened for "leakers" by growing a single colony or a small number of cells (less than about 1000) in YPD, followed by a transfer into YPD containing the drug to which the desired haploids should not be resistant. Only specimens sensitive to this third drug were preserved as a frozen archive and then passaged into the next mating-drive-recombination-sporulation step.

In practice, this procedure included a variety of manipulations. This range of manipulations demonstrates that our method is flexible and can be adapted to work within various technical constraints. For example, when handling few strains, microtiter plates are not necessary and the protocol can be performed in standard culture tubes. In the case of the initial double-mutant mating, for instance, mating was in most cases conducted on YPD-agar patches, which were then scraped and transferred into the YPG diploid selection media. All other matings were conducted in about 90 μL YPD liquid media in wells of 96-well round-bottom microtiter plates. Similarly, selection of haploids after sporulation was sometimes conducted in microtiter plates (128 μL total volume), and other times by streaking to individual colonies on SD-Leu or SD-His agar plates (without 5-FOA counterselection). For all cycles except the experiment's final cycle, individual colonies were isolated and screened at the conclusion. Finally, depending on the scale of the cycle, diploid selection, recombinant selection, presporulation, and sporulation steps were conducted in either microtiter plates (shallow for selections (128 μL media), 2-mL deep-well plates for presporulation and sporulation) or test tubes (5 mL media unless otherwise stated).

Presporulation: Microtiter plate-based presporulation was carried out by pipetting 20 μ L saturated SD-Ura culture into 480 μ L of YPA. Plates were shaken at 1050 rpm at 30°C for 24 hours under a breathable membrane (VWR, 60941-086) before sporulation. Tube-based presporulation was carried out by inoculating 5 mL YPA with 150 μ L saturated SD-Ura culture and incubating on a roller drum at 30°C for 16-24 hours.

Sporulation: Microtiter plate-based sporulation was carried out by pelleting presporulated cells at 2000 g for 2 min, washing by resuspension in 400 µL water, pelleting once again, and resuspending in 400 µL sporulation media. These plates were sealed with a breathable membrane, secured with tape to plate shakers, and shaken at 1350 rpm at room temperature for 4-5 days. Tube-based sporulation was carried out by pelleting tube-presporulated cell cultures and resuspending in 2 mL sporulation media, incubating at room temperature on a roller drum for 3-4 days.

Homozygotes from the final cycle were incubated for 5 generations in YPD+Amp prior to archival freezing, but only after fully selecting for recombination of the landing pad loci with SD-Ura+ β -estradiol.

The final 20 generations of haploid selection in the final cycle were conducted in typical haploid selection media, but lacking lysine, in order to select only for those haploids which retained the barcode next to the LYS2 marker (which segregated in a Mendelian fashion).

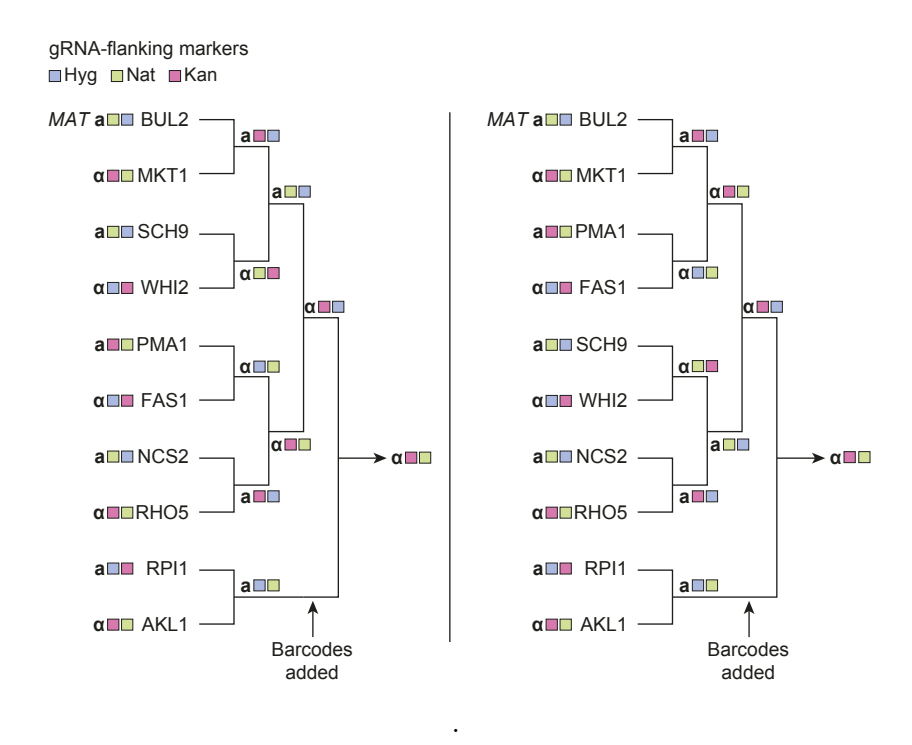


Figure S3: Parallel mating scheme. Biological replicates of the final strains were created via different mating paths.

2 Genotype verification

150

152

153

154

155

156

157

158

159

160

161

162

163

164

165

166

167

168

169

170

171

2.1 Whole-genome sequencing

To verify the lack of systematic off-target Cas9-mediated modifications, and to rule out pervasive aneuploidies, we performed whole-genome sequencing on 96 random clones (3 random wells from each of 32 plates which contained 64 different strains based on the mating procedure outlined in Section 1.5) [53] and sequenced each to approximately 100x coverage. This identified a single case of an euploidy with elevated read counts at three chromosomes that were consistent with disomy [54]. In addition, it identified five credible non-synonymous mutations occurring on more than 1 strain (strongly indicating that the mutations were introduced in the hierarchical mating scheme described in Section 1.5). Two of these (in ERG6 and QRI7) were present in just two strains each, and the other three (in SPT7, HSL7, and FRS1) were present in 5, 6, and 33 strains, respectively. In addition, some extra mutations were identified in single clones, which is not inconsistent given the rate of mutations during meiosis (70% of clones had no mutations, 10% had one, 5% had two, and the rest had poor sequencing coverage leading to what we believe are bad variant calling). These results suggest that Cas9 does not introduce a gross excess of off-target mutations in the genome, and that although unintended mutations do occur in our system (due to Cas9 or meiosis) these mutations are unlikely to dominate the estimation of parameters for modeling the fitness landscape. Notably, as explained in Main Text, biological replicates (independent crosses) were typically in agreement with each other.

To understand whether the mutations in SPT7, HSL7, and FRS1 may have systematic effects on our genotypes, we looked at whether they were present exclusively on any single- or double-mutant backgrounds. We found that the FRS1 mutation was present across most backgrounds, but the

mutations in SPT7 and HSL7 were only present on specific AKL1-RPI1 backgrounds. Notably, fewer than half of the instances of these backgrounds in our WGS data bore these mutations.

2.2 Locus-specific multiplex PCR

To genotype the entire haploid library at all 10 primary loci and 3 putative segregating off-target loci (FRS1, SPT7, and HSL7), we pursued a multiplexed strategy. We began by lysing all 2048 wells (not all of which contained cells) with 20 μL yeast lysis buffer (5mg/mL Zymolyase 20T, 100 mM Sodium Phosphate pH 7.4, 10 mM DTT) and 5 μL of cells straight from the freezer stock. The enzymatic reaction was placed at 37°C for at least 45 min and then at 95°C for 2 min. The released DNA could then be stored in the freezer overnight.

Immediately prior to the first-round PCR, we boiled these products for a minute to mix the lysates. We then added and mixed in $25\,\mu\text{L}$ of water to the lysis products to dilute and facilitate liquid handling. Then, we added $2\,\mu\text{L}$ of this lysis product to the PCR master mix for the first round PCR, mixing after addition. This master mix was for a $25\,\mu\text{L}$ Phire reaction and contained $1.3\,\mu\text{L}$ of pooled $100\,\mu\text{M}$ primers. These primers represented all 13 loci. The 13 primers that added N7 adapters to the amplicons were common across all wells. The 13 primers that added S5 adapters contained 6 bp inline indices. These indices existed in 8 versions, each unique to a different set of 4 plates in the library (54°C annealing, 45s extension). These primers may be found in Data Table S1.

The following day, PCR round 1 products were combined into 4 pools, taking $4\,\mu L$ from each well. We cleaned up these pools with a 1x bead purification step (AMPure beads by Beckman Coulter) (starting volume = $42\,\mu L$, eluted in $35\,\mu L$). We used KAPA polymerase for a second round of $25\,\mu L$ PCRs to anneal unique pairs of S5/N7 indices to the amplicons across 4 reaction plates, using $2\,\mu L$ of purified round 1 product (63°C annealing, 45s extension). Several unsuccessful reactions were repeated as necessary with diluted template.

Round 2 reaction products were then pooled and cleaned via gel extraction, followed by a final bead purification step to remove any remaining small fragments.

The library was sequenced on a NextSeq mid output lane resulting in an average coverage of about 2700x per locus per well in the genotype library. Loci varied in their overall coverage: the average coverage per BUL2 locus was just about 80x, whereas the average coverage for WHI2 was about 7300x. Other than BUL2, all other loci had an average coverage of at least 400x.

Some loci for specific wells were missing from our dataset, or otherwise had very low coverage. To patch these holes in our genotyping data, we amplified with locus-appropriate primers in a first-round reaction to anneal S5/N7 adapters. This reaction used Phire polymerase (54°C annealing, 45s extension) and $2\,\mu\text{L}$ of diluted lysate as template. These reaction products were cleaned up with 1x Ampure beads and eluted in $30\,\mu\text{L}$ water. We took $2\,\mu\text{L}$ of this reaction product into the second round KAPA Hifi PCR reaction, which annealed pairs of S5 and N7 indices unique to each reaction (63°C annealing, 45s extension). Each reaction product was then cleaned up separately using 0.8x Ampure beads on $6\,\mu\text{L}$ of reaction product diluted in $10\,\mu\text{L}$ water. The final product was eluted in $25\,\mu\text{L}$ and pooled for sequencing on a MiSeq Nano lane.

2.3 Counting alleles for each locus in each well

Once we received the Illumina reads, we counted the number of reads of each allele at each locus in each well. To do this, we followed a procedure similar to [25], examining each read in each 8-well sequencing library (corresponding to individual fastq files) in turn. First, we checked that the first 6 bp of read 1 corresponded to a 6-bp inline index, allowing for 1 bp of mismatch. Then, we evaluated

read quality by ensuring that the quality score of the 22bp downstream from the inline index was at least 25. If a read met these conditions, we identified the locus associated with the read by checking for the presence of a characteristic 8-bp sequence either upstream or downstream of the defined allele, allowing identical matches only. For reads matching an identifiable locus, we extracted the 20- to 23-bp allele, sequentially using a list of decreasingly stringent regular expressions (using the python regex module [55]):

'(left 8bp)(length of allele)(right 8bp)',

'(left 8bp)(length of allele-2,length of allele+2)(right 8bp)',

'(left 8bp){e\le1}(length of allele)(right 8bp){e\le1}',

'(left 8bp){e\le1}(length of allele-2,length of allele+2)(right 8bp){e\le1}',

For lists of the exact alleles and 8-bp sequences searched, see Data Table S1.

Overall, fewer than 0.5% of reads were excluded on the basis of these criteria, with no more than 1.2% for a single library.

All alleles that occurred at least 10 times in at least one well AND were present at at least 1% frequency for the corresponding locus in at least one well were given a unique identifier and assigned as either a WT, Mut, or Other allele. "WT" alleles included properly repaired pseudo-WT alleles plus other versions with some or even none of the desired synonymous changes. This includes loci in which it appears no gene drive occurred (i.e., sequences identical to the unmutated parental BY sequence). "Mut" alleles included any with the desired missense change, regardless of the presence or absence of other synonymous alleles. "Other" alleles included those whose amino acid sequence matched neither the WT nor Mut sequence, including errant missense changes and frameshifts. Any remaining alleles were grouped together and designated "na."

2.4 Statistical inference of gene-drive failures

One difficulty of verifying locus correctness by PCR in the final haploid library is that the strains are not clonal (they are derived from the Cas9 gene-drive hierarchical mating procedure, see Section 1.5). Thus, we needed to remove wells that had evidence of a mixture of genotypes, or strong evidence of the incorrect genotype. We noticed that our multiplex PCR verification protocol in Section 2.2 produced evidence of genotype mixtures at a higher rate than anticipated. However, we observed that these supposedly incorrect wells were found more frequently when post-first-round PCR pools were "mixed" at a given locus (i.e., were expected to have both WT and Mut alleles present). This indicated to us that primers from the first-round PCRs were leaking through, thus incorrectly indexing the reads, and/or PCR chimeras were forming.

We developed a statistical model to accurately estimate the true mixture proportion within each well. For each post-first-round pool, we calculated the pool-wide frequencies of all alleles in that pool (based on their unique identifiers). Then, we modeled a pool-wide probability p that a given read is a "true" read and not a chimeric read. We assume that the expected frequency of a false allele in a given well will be (1-p) the poolwide frequency of that allele, whereas a true allele in a given well will have an expected frequency of p + (1-p) the poolwide frequency of that allele. For a range of values of p, constraining p to be at least 50%, we calculated the probability of the data under a multinomial model and obtained the maximum likelihood estimate of p. As necessary, we constrained the likelihood surface to satisfy the constraint that all alleles must be present at a frequency between 0 and 1, inclusive.

After obtaining these adjusted allele frequencies, we set out to distinguish which wells were acceptably versus unacceptably "pure." Since rates of apparent chimera formation varied significantly across loci, we developed a separate purity threshold for each locus. We did this by sorting wells by the percent of non-dominant alleles at a given locus, excluding "na" alleles. We plotted

these proportions against the ascending rank on the x axis, forming a "hockey stick"-like curve that shoots upward at the high end of the distribution. We found the "elbow" of this curve, i.e., the proportion of non-dominant allele at which the curve is furthest from a "hypotenuse" line connecting the end of the handle to the tip of the blade of the proverbial hockey stick. We obtained the following thresholds from this approach:

267 Approximate thresholds

268 BUL2 3.04%, gives 93.3% pure

269 FAS1 1.20%, gives 95.1% pure

270 MKT1 1.13%, gives 96.6% pure

²⁷¹ NCS2 1.94%, gives 96.3% pure

272 PMA1 2.29%, gives 91.8% pure

273 RHO5 1.58%, gives 94.8% pure

274 SCH9 0.64%, gives 94.5% pure

²⁷⁵ WHI2 0.45%, gives 92.9% pure

276 AKL1 3.27%, gives 95.3% pure

277 RPI1 2.36%, gives 95.1% pure

278

279

281

282

283

284

285

286

287

288

289

290

291

292

293

294

295

296

297

298

299

300

301

302

303

304

305

306

For the sake of comparison, we note that overall drive failure rates inferred from sequencing the quadruple and octuple mutants – which was not done in a pooled, chimera-genic way – were close to 2%. In addition, many gene drive events that in fact failed may not be counted here, since a failed drive event that yields the unmutated WT allele when the WT allele is desired will be retained.

All told, 1282 wells matched their expected genotype at all loci (67.8%). Since we had biological replicates of each genotype, 875 out of 1024 possible genotypes (85.4%) were represented among these wells. See Data Table S2 for a complete list of wells, barcodes, and genotypes that passed these filters.

2.5 Other genotyping

In addition to genotyping the final products of the experiment, we genotyped one or more mutated clones per genotype after each cycle of mating, drive, recombination, and selection before proceeding with the next cycle.

Genotyping of the double mutants (after cycle 1) was conducted via Sanger sequencing and visual examination of traces for the expected alleles.

Genotyping of the quadruple mutants (after cycle 2) and octuple mutants (after cycle 3) was conducted via next generation sequencing.

Quadruple mutants were lysed in $50\,\mu\text{L}$ yeast lysis buffer (5 mg/mL Zymolyase 20T (Nacalai Tesque), 1 M sorbitol, $100\,\text{mM}$ sodium phosphate pH 7.4, and $20\,\text{mM}$ DTT), boiled at 95°C for 2 minutes and $2\,\mu\text{L}$ lysed cells were taken into a $25\,\mu\text{L}$ Phire polymerase PCR reaction with $1.25\,\mu\text{L}$ each of the 4 pairs of appropriate primers for 4 loci, respectively (54°C annealing, 30s extension). After this first round of PCR, we purified the product with 0.8x beads and did a second round KAPA Hifi polymerase PCR ($25\,\mu\text{L}$) to append unique S5, N7 indices to each colony isolate. The final product was purified with 0.8x beads once again and sequenced libraries on MiSeq Nano 2x150bp.

Octuple mutants were lysed with $5\,\mu\text{L}$ of saturated culture in $50\,\mu\text{L}$ yeast lysis buffer as previously described. The boiled lysis product was diluted two-fold, $2\,\mu\text{L}$ of the lysis was used in into $24\,\mu\text{L}$ Phire polymerase PCR reaction containing $1\,\mu\text{L}$ of each of $16\,10\,\mu\text{M}$ primers, each of which add the S5, N7 adapter sequences (54°C annealing, 30s extension). Round 1 PCR products were purified via bead cleanup at 0.8x beads ratio, and eluted with $25\,\mu\text{L}$ water. Before cleanup, some

of wells were diluted with an additional $10\,\mu\text{L}$ to bring volume up (evaporation of PCR reactions is frequent), then $12\,\mu\text{L}$ taken as starting volume for cleanup. We then performed the round 2 PCR reaction with unique pairs of S5 and N7 primers for each well, taking $2\,\mu\text{L}$ of cleaned up DNA template into a $25\,\mu\text{L}$ KAPA reaction (63°C annealing, 45s extension time). Round 2 PCR products were diluted with an additional $10\,\mu\text{L}$ water and pooled (3-4 μL of each well). We then performed a 0.7x bead cleanup and submitted the final purified pool for NextSeq Mid throughput 1x150bp lane.

3 Combinatorial indexing and sequencing of barcodes

3.1 Combinatorial pooling and sequencing

To map the barcodes to individual wells, we took a combinatorial indexing approach. Uniquely barcoded AKL1-RPI1 double mutants were cultured in the central 64 wells of 32 96-well microtiter plates (rows A-H, columns 3-10). With the help of a Biomek liquid handler, we took 10 µL of each well-mixed well culture into either of two new 96-well plates, in which wells had been seeded with 30 µL of YPD to facilitate automated liquid dispensing. 70 µL of pooled culture from each well of these two plates was used to form 8 row-specific pools, and the process was repeated form 8 column pools. Each pool contained approximately 1.1 mL of culture. Separately, for each of the 32 plates, 20 µL from each of 64 wells was pooled to form 32 plate pools of about 1.3 mL each.

To prepare libraries for sequencing, we extracted genomic DNA from each of the 48 pools, eluting in 50 μ L water. In an initial PCR step using primers 5xx>pBC1-F and 7xx>pBC2-R, we amplified the barcode loci in each pool, attaching S5 and N7 adapters to each amplicon. For these reactions, we used 0.5-5 μ L of genomic DNA in a 25 μ L Q5 reaction (34 cycles, 54°C annealing, 45s extension). After purifying amplicons via a cleanup with 0.8x ampure beads and eluting into 33 μ L water, we performed a second round of PCR with 1 μ L of purified DNA template and unique pairs of S5 and N7 primers (KAPA 50 μ L reaction, 34 cycles, 63°C annealing, 45s extension). Final PCR products were pooled, with 2 μ L of each plate pool and 8 μ L of each row and column pool (total volume about 200 μ L). Half of this was taken for a 2-sided bead selection, first with 0.5x beads, and next with 0.2x more beads for a 0.7x selection.

Libraries were sequenced on a NextSeq mid-output lane yielding an average coverage of about 8700 reads per barcode per pool.

3.2 Barcode assignment to single wells

Combinatorial indexing allows one to uniquely triangulate a barcode to a specific well. However, errors due to sequencing, apparent cross-contamination due to chimeric reads or lower read coverage for some particular combinatorial pool can make some assignments ambiguous. We therefore performed this assignment using a greedy procedure. First, barcodes that uniquely map to a single well were identified. This yielded 2332 barcodes (out of 2348) that mapped to 2029 wells. Evidently, some wells contained multiple barcodes that stem from imprecise colony picking. 16 barcodes appeared to map ambiguously to multiple wells. Manual inspection found that 12 of these could be explained by spurious reads in other pools, which meant we only had to remove four wells with conflicting barcodes.

We additionally found about 40 wells that appeared to grow extremely slowly in SD-Ura+ β -estradiol+Amp, perhaps due to picking petite colonies. All were of the same AKL1-RPI1 genotype (AKL1 176S, RPI1 102D) and from the same barcode transformant pool, leading us to believe this may be due to private mutations in one of the 5 replicate pooled colonies. We manually identified,

removed, and repicked these remaining wells from the opposite transformant pool of that same AKL1-RPI1 genotype, in which we had seen no issues. In addition, we repicked about a dozen barcode transformant colonies for wells with unassigned barcodes.

The second set of barcodes was assigned again by combinatorial indexing, this time with only 8 rows and 8 columns, and some spurious remaining wells that did not have a well-defined barcode were also confirmed by Sanger sequencing.

357 4 Bulk phenotyping

4.1 Growth experiments

The complete frozen pool was grown in 5 mL YPD by inoculating approximately 10^7 total cells to produce the starting population. We then diluted these populations by $1:2^7$ daily by passaging 781 µL into 5 mL fresh media (of some particular environment) in 15 mL culture tubes on roller drums. Whole population pellets, obtained from 1.5 mL of saturated culture, were stored immediately at -20°C for later sequencing. As previously described [31], this protocol results in about 7 generations per day, with a daily bottleneck size of about 10^8 in most assay environments. We performed two replicates of each assay and sampled for 49 generations (7 timepoints). Only 5 timepoints (representing 7, 14, 28, 42, and 49 generations) were sequenced.

The six environments chosen were: YPD + 0.4% acetic acid (YPDA), YPD + 6 mM guanidium chloride (gu), YPD + 35 μM suloctidil (suloc), YPD + 0.8 M NaCl (salt), YPD at 37°C (37C), and SD + 10 ng/mL 4NQO (4NQO). (All environments besides 37C were at 30°C.) The YPDA environment was chosen because preliminary experiments suggested that it had a tendency to reveal phenotypic variance and it previously had been studied in our lab ([31]). Gu was chosen because of its known large target size from separate work in our lab which identified a change in sign for the effect of the MKT1 D30G mutation. Suloc and 4NQO were chosen because previous work in our lab showed these environments to have low genotype correlation with other YPD-based environments. 37C and salt were chosen because several of the genes under study were previously reported to be mutated in evolution under that stressor or be a QTL in that stressor (NCS2 in high temperature; PMA1, RPI1, and RHO5 were all mutated in NaCl evolution experiments; see Table 1.2).

The degree of the stressor in suloc, YPDA, salt, and 4NQO environments was chosen empirically to maximize the stress while still permitting 7 generations of growth per day over the entire phenotyping assay.

4.2 Amplicon barcode sequencing

Genomic DNA from cell pellets were processed as in [31]. Briefly, DNA was obtained by zymolyase-mediated cell lysis (5 mg/mL Zymolyase 20T (Nacalai Tesque), 1 M sorbitol, 100 mM sodium phosphate pH 7.4, 10 mM EDTA, 0.5% 3-(N,N-Dimethylmyristylammonio)propanesulfonate (Sigma, T7763), 200 μg/mL RNAse A, and 20 mM DTT) and binding on silica mini-preparative columns with guanidine thiocyanate buffer (4 volumes of 100 mM MES pH 5, 4.125 M guanidine thiocyanate, 25% isopropanol, and 10 mM EDTA). After binding, the columns were washed with a first wash buffer (10% guanidine thiocyanate, 25% isopropanol, 10 mM EDTA) and then a second wash buffer (80% ethanol, 10 mM Tris pH 8), followed by elution into elution buffer (10 mM Tris pH 8.5). 1.5 mL of pelleted cells eluted into 100 μL routinely provided about 1-2 μg of total DNA.

PCR of the barcodes was performed using a two-stage procedure previously described to attach unique molecular identifiers (UMIs) to PCR fragments (see [31] for a detailed protocol). Primers used in the first-stage PCR contained a priming sequence, a 7-12-nucleotide multiplexing index,

8 random nucleotides as UMIs, and an overhang that matched the Tn5 transposome. These two primers had the configurations P1 = TCGTCG GCAGCG TCAGAT GTGTAT AAGAGA CAGNNN NNNNNY YYYYYYY AAGGTA CGATTC TGACGC A, P2 = GTCTCG TGGGCT CGGAGA TGTGTA TAAGAG ACAGNN NNNNNN YYYYYYY YAGTTG TCTCTG CTCTCG CTA. Here N corresponds to degenerate bases used as UMIs, and Y corresponds to multiplexing indexes.

These primers anneal on either side of the barcode sequence integrated just downstream of LYS2, at the pBC1 and pBC2 sites, respectively. After attachment of molecular identifiers to template molecules during three PCR cycles ($20\,\mu\text{L}$ Q5 Polymerase reaction, 50°C annealing, 30s extension), the first-stage amplicons were cleaned using Ampure beads using an automated liquid handling protocol established for a Biomek FXp, with 1.25x Ampure beads, eluting in $35\,\mu\text{L}$. Of the elution of this clean-up, $30\,\mu\text{L}$ was used directly as template for the second-stage PCR with primers that contained multiplexing indexes and adapters that anneal to the Illumina flowcells (P5 and P7 primers). After 35 PCR cycles ($50\,\mu\text{L}$ KAPA Hifi Polymerase reaction, 63°C annealing, 30s extension), these final products were then purified using Ampure beads, quantified, and pooled to approximately equimolar concentration. The PCR products were sequenced with a NovaSeq S1 full flow cell (Illumina) by paired-end sequencing (2 x 50 bp, reading 80 bp from the P1 direction and 20 bp from the P2 direction).

We first processed our raw sequencing reads to identify and extract the indices and barcode sequences as in [31]. Using the barcodes previously identified in Section 3.2, we can make "corrections" to reads with sequencing errors by direct lookup of the lowest Levenshtein distance to the dictionary of verified barcodes.

Finally, we can calculate the counts of each error-corrected true barcode by removing duplicate reads, using the unique molecular identifiers from the first-stage PCRs. Frequencies calculated from these counts are used to infer fitnesses for all segregants, as explained in Section 4.3. After all filtering, our final mean sequencing coverages were over 1500 reads per barcode per timepoint per replicate (averaged across all assays).

4.3 Fitness inference for time-dependent barcode frequencies

Strain fitnesses can be inferred from relative barcode frequencies over time (see Refs. [31] and [56] for expanded information on joint inference of fitnesses using barcode frequencies). Briefly, fitnesses are regressed as the change in relative log frequencies of strains against a selected reference per generation. This parameter is approximately the difference in instantaneous growth rate between lineages under exponential growth. Most genotypes in our data are represented by more than one barcode in the same assay (representing biological replicates), and each barcode was measured in two technical replicates. In theory, we could jointly infer the biological replicates and constrain their fitnesses to be equal. This would yield, for a combinatorially complete landscape, exactly 2^N fitnesses which could be fit exactly with 2^N coefficients (later described in Section 5.1). However, strains with the same desired genotype may not always be identical at all other loci in the genome (due to new mutations or off-target effects). By only performing the joint inference on technical replicates, variance left unexplained by a full model containing 2^N coefficients can be regarded as biological variation at other loci and some measurement error (described in more detail in Section 5.2). This joint inference is intuitively similar to a weighted average of the two technical measurements, with weights proportional to the evidence within each replicate (which is a combination of the number of reads and the number of timepoints measured). A standard error for the inferred fitness parameter can be obtained through the inference process by the square root of the inverse of the Fisher information at the maximum likelihood. This standard error can be interpreted as the error that can be attributed to the (overdispersed) binomial sampling error. For our analyses, we removed datapoints with standard error above 1.

4.4 Comparison between technical, biological replicates

As shown in Figure S3, biological replicates were made for all final strains in the experiment by proceeding through a parallel mating scheme. However, due to gene-drive failures, some strains were not found in replicate, and it may be useful to ask the following questions: 1) How trustworthy are the strains without replicates? and 2) What is the average effect of unintended mutations introduced within our cross? To answer these questions, we can compare the inferred fitnesses of technical (comparing the same barcode across assays) and biological replicates (comparing barcodes that correspond to the same expected genotype).

Decomposing the observed phenotypic variance due to measurement error can be done by the standard reliability estimates. The Pearson's correlation coefficient between two technical replicates is an estimate of the \mathbb{R}^2 between the true fitness value and one fitness measurement for the barcode. If one takes the mean of the r technical replicates, then:

$$\frac{\sigma_{err}^2/r}{\sigma_{qen}^2 + \sigma_{err}^2/r} = \frac{1 - \langle \rho_{r_i, r_j} \rangle}{1 + (r - 1)\langle \rho_{r_i, r_j} \rangle}.$$
 (1)

Decomposing the phenotypic variance due to extra variance in the genetic component can be done by a similar process, by comparing the measurement values between strains bearing different barcodes but expected to have the same genotype. Here, to perform this calculation, we constrain ourselves to pairs of strains with the same genotype that each have a single barcode in their well so that a single comparison can be made. The correlation coefficient between biological replicates can be interpreted in a similar way to technical replicates, but the deviation from 1 here will reflect both error due to extra variation in the genome and error due to measurement error (but without tube-to-tube variation). For the purpose of our manuscript, we assume that this tube-to-tube variation is negligible.

In plots of technical and biological replicates, density-based coloration was determined by calculating each point's mean distance to its five nearest neighbors. Distances were transformed using the scikit MinMaxScaler() function and plotted with normalized colors based on a reversed viridis colormap.

Technical and biological replicate comparisons for all data can be viewed in Fig. S4.

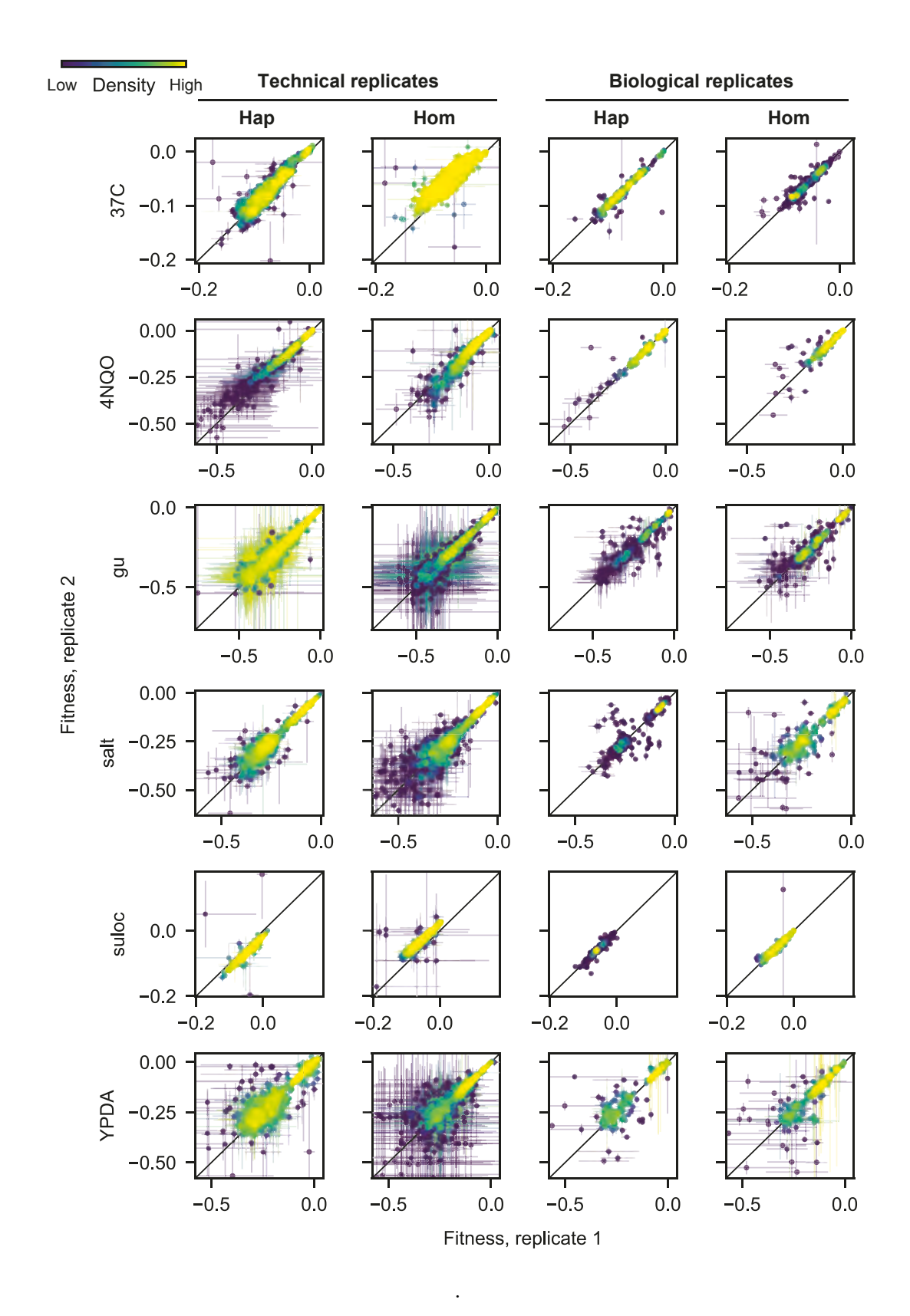


Figure S4: Comparison of technical and biological replicates for all ploidies and assay environments

5 Quantitative analysis of epistasis

5.1 Estimation of parameters

We model fitness ϕ as a function of the the underlying genotype which can be expressed as a sum of combinations of N biallelic loci x_1, x_2, \ldots, x_N that take on values $x_i = \pm 1$.

$$\phi = \overline{\phi} + \sum_{i} s_i x_i + \sum_{i>j} s_{ij} x_i x_j + \sum_{i>j>k} s_{ijk} x_i x_j x_k + \dots$$
 (2)

This modeling framework casts additive first-order terms as the background-average effect of the mutation, which is distinct from the effect of the mutation on some arbitrary wild-type genotype. The terms s represent half the fitness difference between groups of individuals with and without the mutation, or alternatively the expected deviation from the mean, positive or negative, for groups with or without the mutation respectively. Pairwise epistatic effects are the background-average perturbation that can be fit beyond the additive first-order term, and higher order epistatic terms are similarly modeled. This view offers several advantages: 1) if one decides to choose a particular genotype as the "wild-type", only the signs of the terms need to change; 2) each coefficient is estimated by partitioning half of the genotypes (each coefficient corresponds to a distinct slice of the data), meaning each coefficient is equally powered; and 3) the coefficients are in principle orthogonal from each other (there is no expected collinearity between the genotypic values of any pair or combination of coefficients). This means that there is no "order" of coefficient fitting (one does not have to fit the additive terms first), and fitting one coefficient does not influence another.

Coefficients from the equation above can always be estimated by least-squares regression when all 2^N genotypes have a phenotypic measurement, though we note that we have in practice on average more than 1 phenotypic measurement per genotypes due to our biological replicates. However, we may expect this formula to be sparser: not all mutations should have an effect, and not all pairs of mutations should have a pairwise epistatic effect. We can regularize the estimation procedure to yield a sparse subset using the LASSO procedure, which penalizes the least-squares regression by the sum of absolute magnitudes of coefficients:

$$\min_{s} \left\{ ||\phi - \hat{\phi}||_{2}^{2} + \lambda ||s||_{1} \right\}.$$
 (3)

In the absence of collinearity (as stated above, our formulation has no collinearity between parameters), the LASSO operation is known to be consistent and asymptotically selects the correct subset of non-zero parameters [57]. Sparsity is controlled by the λ parameter, which can be found by cross-validation (in our case, 5-fold cross-validation was performed to reduce the extent of overfitting). This approach removes coefficients that are approximately the same scale as the noise. To provide 95% confidence intervals on the LASSO estimates, we performed 500 bootstrap resampling with replacement of the data followed by model selection.

As discussed previously in Section 2.1, we identified extra mutations present in multiple strains (FRS1, SPT7, HSL7). Because the SPT7 and HSL7 mutations likely occurred during the mating process (Section 1.5), they may lead to specific signals of epistasis if they themselves have an effect. We briefly assessed this possibility by plotting the distribution of fitnesses for individuals with and without the mutation (constraining on the backgrounds in which the mutations were identified). In visually examining these plots, we were unable to find evidence of a systematic effect for these mutations. Therefore, these mutations were removed from consideration before building the model by LASSO. On the other hand, FRS1 was likely present in one of the original parents of the experiment and thus was found in approximately 50% of final strains. Though we did identify a

possible effect for this mutation in some environments, because it is not systematically distributed across the library, it is only expected to affect one of the higher order epistatic terms. (We cannot distinguish the effect of the epistatic term for the combination of strains that have FRS1 mutated and the effect of the FRS1 mutation). However, note that we have produced strains in replicate. Thus, the effect of the FRS1 mutation is unlikely to be consistently found in the same strains, and its signal will therefore be unlikely to dominate the epistatic term.

In general, the broad-sense heritability captured by the model is very high as both biological and technical replicates show high correlation (see Fig. S4). Thus, correlation of fitness measurements between environments can reveal the similarities between model coefficients. If measurement noise was too great such that it would dilute the correlation coefficients, then comparison between the predicted fitnesses may provide a better picture of environmental similarities (given that the coefficients were adequately estimated).

5.2 Variance partitioning

The phenotypic variability in the dataset can be partitioned into various components to quantify their relative importance. In our experiment, we are interested in not just the broad-sense heritability due to our focal loci (H^2 , or the variability due to genetic components), but also in the heritability due to specific additive and epistatic components. When the model coefficients are orthogonal, the phenotypic variance due to genetic components is trivially obtained by the sum of squares of each coefficient:

$$\sigma_{\text{gen}}^2 = \sum_{i} s_i^2 + \sum_{i>j} s_{ij}^2 + \sum_{i>j>k} s_{ijk}^2 + \dots$$
 (4)

Partitioning the variance by subsets of coefficients – for example partitioning by first order terms or pairwise epistatic terms – is therefore straightforward.

$$\sigma_{1\text{st}}^2 = \frac{\sum_i s_i^2}{\sigma_{\text{gen}}^2} \tag{5}$$

$$\sigma_{\text{2nd}}^2 = \frac{\sum_{i>j} s_{ij}^2}{\sigma_{\text{gen}}^2} \tag{6}$$

However, we note that the coefficients are estimated from the data, and variance partitioning in this manner produces a bias. Removal of this bias is the major motivation behind mixed linear models that estimate narrow-sense heritability [58]. This caveat is not a major concern for our study, though, since extra sources of variation are either negligible (all the phenotypes are measured simultaneously in the same tube) or can be well estimated (measurement error can be estimated by replication). None of these extra sources of variation are expected to fundamentally alter only some of the coefficients or some subset of coefficients, and thus these relative partitions are expected to be unbiased.

6 Analysis of fitness-correlated trends

All epistatic interactions are ultimately the consequence of biophysical, physiological, or functional interactions, which depend on the specific details of the mutations involved. However, recent work has suggested that overall statistical patterns of epistasis follow regular and predictable fitness-mediated trends. In this section, we describe the framework we use to study these fitness-correlated

trends, and analyze the extent to which they can emerge as the consequence of specific idiosyncratic interactions, instead of from "global" effects involving non-specific fitness-mediated interactions among mutations.

6.1 Fitting regression slopes to determine fitness-correlated trends

Fitness-correlated trends (FCTs), such as diminishing returns or increasing costs, have often been analyzed by regressing the fitness effect of a mutation, $s = \Delta \phi = \phi_{mut} - \phi_{wt}$, against the fitness of the background in which it occurs, ϕ_{wt} . We refer to this as the $\Delta \phi$ formulation: we say that there is no FCT if $\Delta \phi$ is constant over a wide range of background fitness, while a negative relationship between $\Delta \phi$ and ϕ_{wt} corresponds to diminishing returns/increasing costs (and a positive relationship corresponds to increasing returns/diminishing costs). However, care must be taken when performing this analysis, because when we regress $\Delta \phi$ against ϕ_{wt} , measurement errors in ϕ_{wt} will lead to a negative correlation even in the absence of true fitness-correlated trends [59].

A further complication with this formulation is that the regression slope we obtain depends in a complex way on the polarization we choose for the mutation (i.e., which allele is considered the wild-type and which is the mutant). To see this, consider the following simple linear model for $\Delta \phi$ as a function of ϕ_{wt} :

$$\Delta \phi \equiv \phi_{mut} - \phi_{wt} = a_1 + b_1 \phi_{wt},\tag{7}$$

and the analogous model for the fitness effect of the reversion, $\Delta \tilde{\phi}$, as a function of ϕ_{mut} :

$$\Delta \tilde{\phi} \equiv \phi_{wt} - \phi_{mut} = a_2 + b_2 \phi_{mut}. \tag{8}$$

Fitting data to these models using standard methods for ordinary least-squares, we find that the relationship between the regression slopes b_1 and b_2 is given by

$$b_2 = -\frac{b_1 + V}{1 + 2b_1 + V},\tag{9}$$

where we have defined

$$V = \frac{\text{Var}[\Delta \phi]}{\text{Var}[\phi_{wt}]}.$$
 (10)

We can use these equations to gain some intuition for the effect of V on the regression slopes and their reversions (i.e., a change in polarization). First, $V \geq 0$ by construction, and V = 0 only if there is no measurement error or no idiosyncratic epistasis, which in some extreme cases could be interpreted as measurement error for all measurements. As expected, it is only possible to lack an FCT in both polarizations ($b_1 = b_2 = 0$) if V = 0. Of note, the numerator of V can be decomposed to $\text{Var}[\phi_{mut}] + \text{Var}[\phi_{wt}] - 2Cov(\phi_{mut}, \phi_{wt})$, which shows that without a specific relationship between fitnesses of individuals with and without the mutation, V > 0, and an FCT will always emerge in at least one of the two polarizations.

Since in practice V is always positive, we can see that, as shown in Figure S5 and from Equation 9, when $b_1 \geq 0$, then $b_2 < 0$, no matter the difference in scale of V and b_1 . Thus, in practice, increasing returns (or diminishing cost) epistasis or no FCT in one polarization of which allele is the "WT" always shows as diminishing returns (or increasing cost) in the reversion (when the allele is considered to be the "Mut" instead).

When $b_1 < 0$, or when there is diminishing returns in this polarization, then the behavior of b_2 depends on the scale of b_1 and V. First, some scenarios lead to $b_2 = 0$, or no FCT in the reversion, and these scenarios occur at the critical boundary where $V = -b_1$. Another critical boundary occurs where $V = -1 - 2b_1$, which leads to an asymptotic boundary where $b_2 \to \pm \infty$.

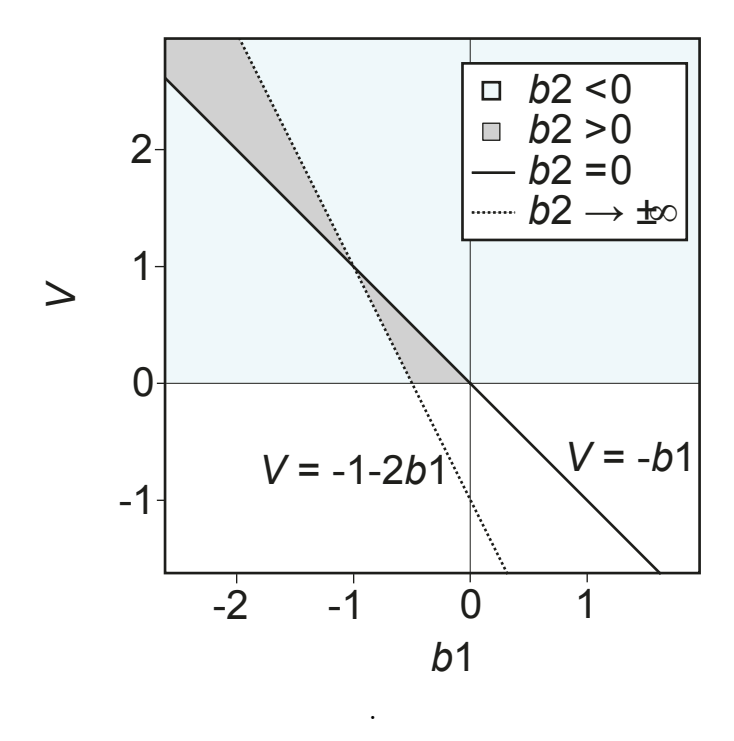


Figure S5: Relevant regimes for slopes and their reversions in the $\Delta \phi$ formulation. V is from Equation 10, b_1 and b_2 are least-squares regression slopes when an allele is labeled as the WT allele or the mutated allele (i.e., the reversion).

When $b_1 < 0$, only a small region between the critical boundaries leads to $b_2 > 0$ (the reversion is increasing returns or diminishing cost epistasis). Outside the critical boundaries, $b_2 < 0$ and therefore diminishing returns or increasing costs is found in both polarizations of the allele. Thus, across the full space of possible parameters, diminishing returns and increasing costs – both of which present as a negative regression slope – are more likely to emerge than positive regression slopes in this $\Delta \phi$ formulation (though we note that biology may not explore this entire parameter space uniformly), and slopes when mutations are reverted cannot always be anticipated intuitively. We can also ask when $b_2 = b_1$: this will happen when $b_1 = -0.5V$. Because $V \ge 0$, this will only happen when $b_1 < 0$ (and therefore $b_2 < 0$). Another fact from this equality is that if $b_2 = b_1$, then the denominator of V has to be equal in the reversion. This means that $b_2 = b_1$ implies $Var(\phi_{wt}) = Var(\phi_{mut})$.

Note, these complications are still present when using other regression techniques such as total least squares that take into account measurement errors in ϕ_{wt} and ϕ_{mut} [41].

In contrast, we can resolve some of these complications by making two changes to the analysis: (1) plotting ϕ_{mut} directly against ϕ_{wt} , and (2) regressing a linear relationship based on the total least squares. Firstly, this approach avoids some problems with correlation in measurement errors. In this formulation (i.e., the ϕ_{wt}/ϕ_{mut} formulation), measurement errors in both strains (or errors in the dependent and independent variable) are taken into account [41] (we use the standard errors estimated from Section 4.3), and we have the model functions:

$$\phi_{mut} = a_3 + b_3 \phi_{wt} \tag{11}$$

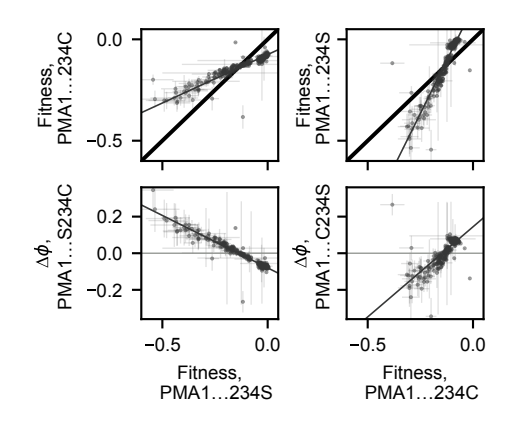


Figure S6: Comparison of fitness correlated trends for a simple case where the reversion of the focal mutation is straightforward. Haploid, 4NQO environment.

and the reversion:

$$\phi_{wt} = a_4 + b_4 \phi_{mut} \tag{12}$$

Secondly, this framing and regression method (taking into account errors in both axes) also behaves far more intuitively: the slope in one direction is always the reciprocal of the other (i.e., $b_3 = 1/b_4$).

To obtain some intuition of how to interpret FCTs in this ϕ_{wt}/ϕ_{mut} formulation, we can first attempt to interpret $b_3 = 1 = b_4$. This only occurs if $\text{Var}(\phi_{wt}) = \text{Var}(\phi_{mut})$, a property of the regression method. As described earlier, this is the regime where $b_1 = b_2 \leq 0$, and $b_1 = b_2 = 0$ only if $\text{Var}(\phi_{mut} - \phi_{wt}) = 0$. Thus, a caveat of this ϕ_{wt}/ϕ_{mut} formulation is that a slope of 1 does not always indicate the absence of an FCT. In contrast, when $b_3 \neq 1$, then either $b_1 \neq 0$ or $b_2 \neq 0$. This can be shown by the fact that $b_3 \neq 1$ only when $\text{Var}(\phi_{wt}) \neq \text{Var}(\phi_{mut})$. This case necessarily implies $\text{Var}(\phi_{mut} - \phi_{wt}) \neq 0$, which is the necessary condition for V > 0.

We summarize these behaviors with some example figures from our data. First, we show an example of intuitive behavior, comparing both regressions and with mutational reversions (Figure S6). In this simple example, regression of the fitness effect of the PMA1 234C mutation leads to a case of diminishing returns and increasing cost epistasis. When the mutation is "reverted," or we regress the effect of the 234S mutation, we obtain the opposite FCT (diminishing costs, or increasing returns). These trends are also well-captured in the ϕ_{wt}/ϕ_{mut} formulation.

On the other hand, many examples are far less intuitive (Figure S7). In this example, regressing the effect of the WHI2 262L mutation leads to diminishing returns. However, regressing the effect of the reversion (262S) also leads to diminishing returns. In the ϕ_{wt}/ϕ_{mut} formulation, slopes behave as expected (the reversion is the reciprocal).

Examples where FCTs can only be interpreted in one of the mutational orientation are also found (Figure S8). In this example, the PMA1 234C mutation apparently shows no FCT, while its reversion displays increasing cost epistasis. On the other hand, the ϕ_{wt}/ϕ_{mut} formulation robustly shows a slope different from 1 and again behaves as the reciprocal when the mutation is reverted. Thus, because different slopes in this formulation do not readily yield an interpretation of the type of FCT (diminishing returns vs increasing returns), we refrain from using these plots for this purpose. Instead, we focus on this formulation's ability to robustly identify FCTs when it exists.

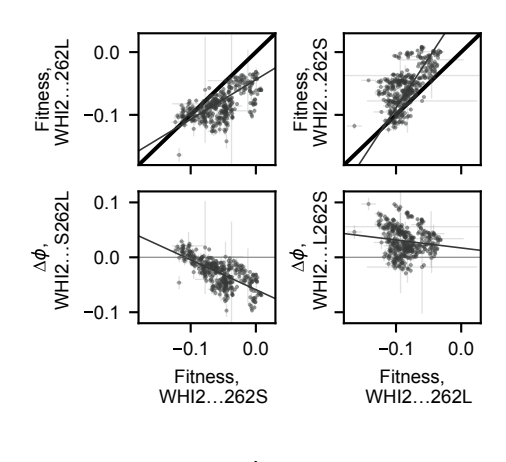


Figure S7: Comparison of fitness correlated trends for a complicated case where the reversion of the focal mutation is not intuitive. Haploid, high-temperature environment.

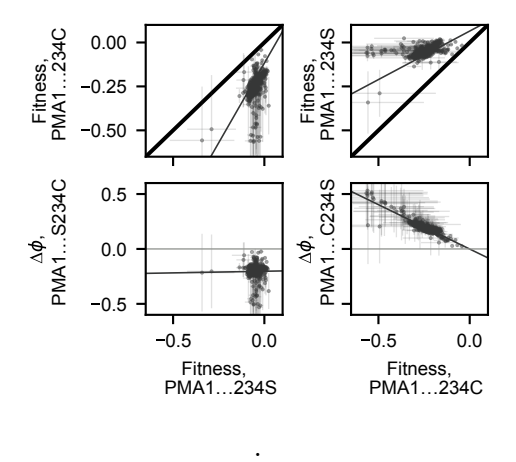


Figure S8: Comparison of fitness correlated trends for a case where reversion may be interpreted as having no FCT. Haploid, acetic acid environment.

For our analysis, a final complication emerges from having biological replicates. In the parameter estimation above (Section 5.1), this does not pose a problem (there is simply unexplained variation). However, for the purpose of analyzing fitness correlated trends, if strains have two replicates for the wild-type and two replicates for the mutant, then there are 4 possible comparisons and it is no longer clear how to regress this effect of the mutation. To resolve this, we perform the analysis on the average fitness of each genotype, which can be interpreted as the best estimate of the true fitness of the genotype. The standard error of the average genotype fitness was computed as the mean of the errors associated with the fitnesses that were averaged.

We have shown that, in general, if slopes different from 1 are obtained in the ϕ_{wt}/ϕ_{mut} formulation, then we can interpret the data as displaying FCTs. However, what yields slopes different from 1? If these formulations are readily interchangeable, then we may expect a single idiosyncratic epistatic term involving the focal mutation, positive or negative, to be sufficient. However, we find that this is not the case: in this formulation, we find that this epistatic interaction must also involve a mutation with a non-zero additive effect.

To illustrate this, we begin with a simple schematic considering two loci A and B on top of a background of other mutations with some fitness variance (Figure S9). We denote alternative alleles at these loci as their letter case (A/a, and B/b), and the deviation from the mean fitness between genotypes of alternative alleles for locus A as: $s_A = \phi_A - (\phi_A + \phi_a)/2$. When $s_A = 0$, $s_B = 0$, and $s_{AB} = 0$, then plotting ϕ_A vs ϕ_a must yield a general "cloud" of points with a slope of 1 (Figure S9, top left panel). Partitioning the cloud of points by genotypes with the B and b alleles. respectively, only yields two superimposed clouds (because the effect of having the mutation at locus B, s_B , is zero). When $s_A = 0$, $s_B \neq 0$, and $s_{AB} = 0$, then the two clouds separate themselves along the 1:1 line (Figure S9, top right panel). The regression slope for ϕ_A vs ϕ_a is still 1. The case where $s_A = 0$, $s_B = 0$, and $s_{AB} \neq 0$ is more complicated. Setting $s_{AB} = E$, a constant, we find the mean deviation in fitnesses $\phi_{AB} = E$, $\phi_{aB} = -E$, $\phi_{Ab} = -E$, and $\phi_{ab} = E$. If we focus on plotting ϕ_{ab} against ϕ_{Ab} , we find that the negative deviation due to the epistatic coefficient for ϕ_{Ab} moves the cloud to the left, while the positive deviation due to the epistatic coefficient for ϕ_{ab} moves the cloud up. These coordinated movements yield a diagonal movement orthogonal to the 1:1 line. The same logic can be applied to plotting ϕ_{aB} against ϕ_{AB} , however in this case the cloud moves to the right and down. Thus, the two clouds separate themselves in the direction of a slope of -1 when an epistatic term is present (Figure S9, bottom left panel). The regression slope for ϕ_A vs ϕ_a is still 1 even in this case and will eventually flip to be -1 as clouds separate themselves farther and farther. Putting these orthogonal movements together, we find that the non-zero terms for $s_A = 0$, $s_B \neq 0$, and $s_{AB} \neq 0$ lead to joint cloud movements (Figure S9, bottom right panel). The regression slope for ϕ_A vs ϕ_a in this final case will never be one. Because these conditions include the sufficient condition for FCTs in the $\Delta \phi$ formulation, our analyses on FCTs with this ϕ_{wt}/ϕ_{mut} formulation are conservative, and we use this formulation for its advantages: 1) errors in fitness measurements are taken into account for both ϕ_{wt} and ϕ_{mut} , 2) the slope for the mutation reversion is the reciprocal, and 3) slopes different from 1 are always FCTs.

6.2 Decomposition of fitness-correlated trends

626

627

628

629

630

631

632

633

634

635

636

637

638

639

640

641

642

643

645

646

647

648

649

650

651

652

653

654

655

656

657

658

659

660

661

662

663

664

665

666

667

668

670

To understand whether idiosyncratic interactions lead to fitness-correlated trends, we proceeded down two analytical avenues.

In the first, we examined the observed genotype fitnesses and removed epistatic terms one at a time to see whether slopes converged to 1. Operationally, this involved first finding the global linear regression line that fit the data best for a given locus in a given ploidy and environment. We compared that regression to the best-fit line with slope of 1 by looking at the weighted sum of

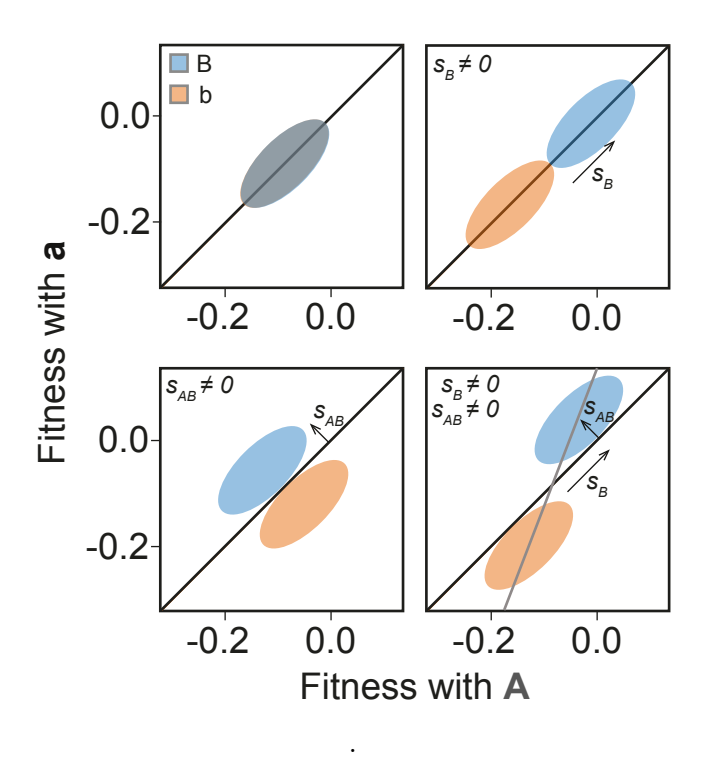


Figure S9: Effect of parameters on global regression in the ϕ_{wt}/ϕ_{mut} formulation. Clouds shown are for when $s_A=0$. Top right shows the effect of $s_B\neq 0$, bottom left shows the effect of $s_{AB}\neq 0$ and bottom right shows the effect of both $s_b\neq 0$ and $s_{AB}\neq 0$.

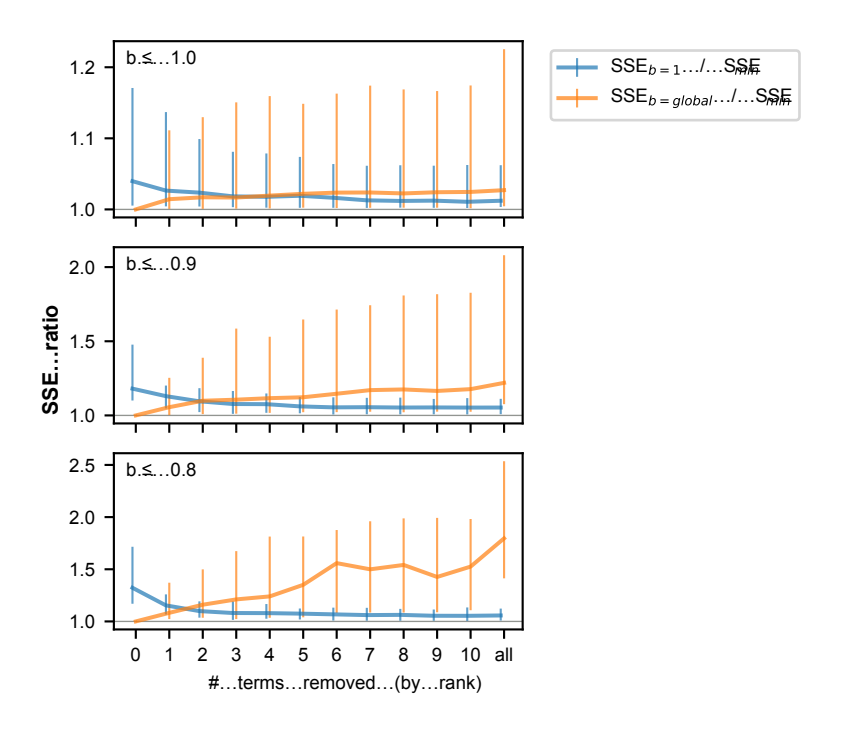


Figure S10: Three panels, one for each b threshold, showing the change in the ratios of the SSE for lines of slope b = 1 and b =global as compared with the SSE for an unconstrained regression that minimizes SSE. Vertical bars indicate interquartile ranges.

squared errors (SSE), where a lower sum indicates a better fit to the data. After doing this, we found the residual difference between the observed genotype fitnesses and the genotype fitnesses as predicted by our full model of additive and epistatic terms. Then, we set the largest epistatic term involving the focal locus to zero, regenerated the model fitness values, and added the residual differences. To this dataset, we fit a line with the original global slope and a line with the slope 1, again finding the SSE for each. We also fit a totally new regression line that minimized the SSE. We then iterated this process, consecutively removing 10 epistatic terms and re-evaluating the fit of the b=1 and b=global lines each time. Main text Figure 3E shows how the relative fit of these two lines changes across ploidies, environments, and loci. Figure S10 shows how the SSE for b=1 and b=global compare to the minimized SSE as terms are progressively removed, revealing that a slope of 1 tends to approach an idealized fit as terms are removed, while the global slope tends to drift away. Figure S11 provides a more detailed look at how the ratio of SSEs for b=1 and b=global change as terms are removed for each locus in each ploidy and environment.

In a converse analysis, we examined genotype fitnesses generated by our model of additive and epistatic terms. For a focal locus in a given ploidy and environment, we first stripped away all epistatic terms related to interactions between the focal locus and other loci, such that only additive terms and interactions among background loci contributed to the modeled genotype fitnesses. This produced a perfectly straight line with a slope of 1 and an intercept proportional to the background-averaged additive effect of the focal mutation (as described in Section 5.1, this is twice the estimated parameter s_i where i is the focal locus). We ranked the epistatic terms involving the focal mutation by their effect size. Then, starting with the largest, we incorporated one term at a time into the modeled genotype fitnesses. After each term was added, we replotted the fitness of genotypes with

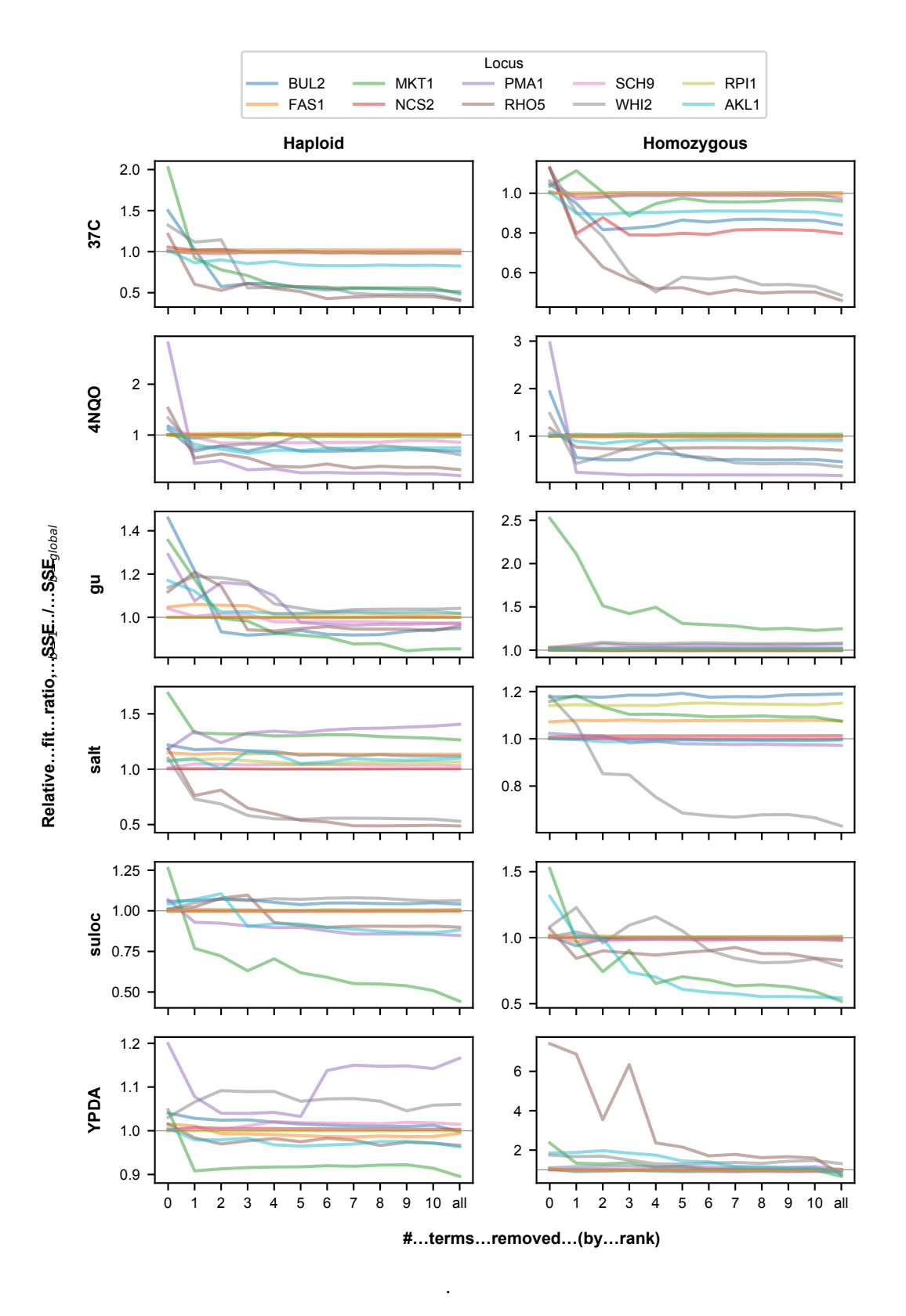


Figure S11: One panel for each ploidy and assay environment showing the change in the ratio of the SSEs for lines of slope b = 1 and b =global for each locus.

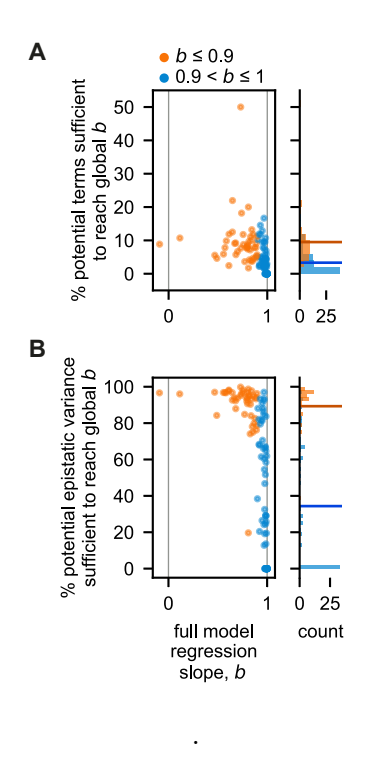


Figure S12: Scatterplot and histograms of regression slopes of FCTs for all data and the percentage of inferred epistatic (A) terms and (B) variance needed to recapitulate them. Horizontal colored lines in the histogram illustrate the mean.

and without a mutation at the focal locus and computed the regression slope.

We defined the number of terms sufficient to recapitulate the observed FCT as the number of added terms required to reach regression slope convergence within 0.01. More specifically, after adding each term, we asked whether the new regression slope differed from each of the previous three regression slopes by less than 0.01. If so, the number of terms required to reach that "plateau" was considered the number of terms sufficient to recapitulate the observed FCT. In a minority of cases, the final "plateau" slope differs from the full-model slope by greater than 0.01, but only in 5 instances by greater than 0.02. Figure S12 presents the fraction of potential epistatic terms and potential epistatic variance sufficient to reach this plateau.

Note that, to permit more consistent comparisons, all loci were analyzed in the mutational direction that placed their regression slopes between -1 and 1. In other words, if plotting genotype fitness with A on the x axis and genotype fitness with a on the y axis gave a slope greater than 1, we would flip the axes such that the slopes would be equal to the reciprocal of the original slope (between 0 and 1).

Plots of ϕ_{wt}/ϕ_{mut} for all loci can be found in Figure S13 and Figure S14.

6.3 Quantifying the effect of landscape size in the analysis of fitness-correlated trends

The size of the fitness landscape we consider has two important effects on our ability to analyze the origins of fitness-correlated trends. First, as the number of mutations involved increases, the number of potential epistatic interactions between them increases exponentially. This creates more opportunities for idiosyncratic interactions to exist and to produce apparent fitness-correlated trends. We note that this is an average effect: if we happened to choose precisely the set of mutations that

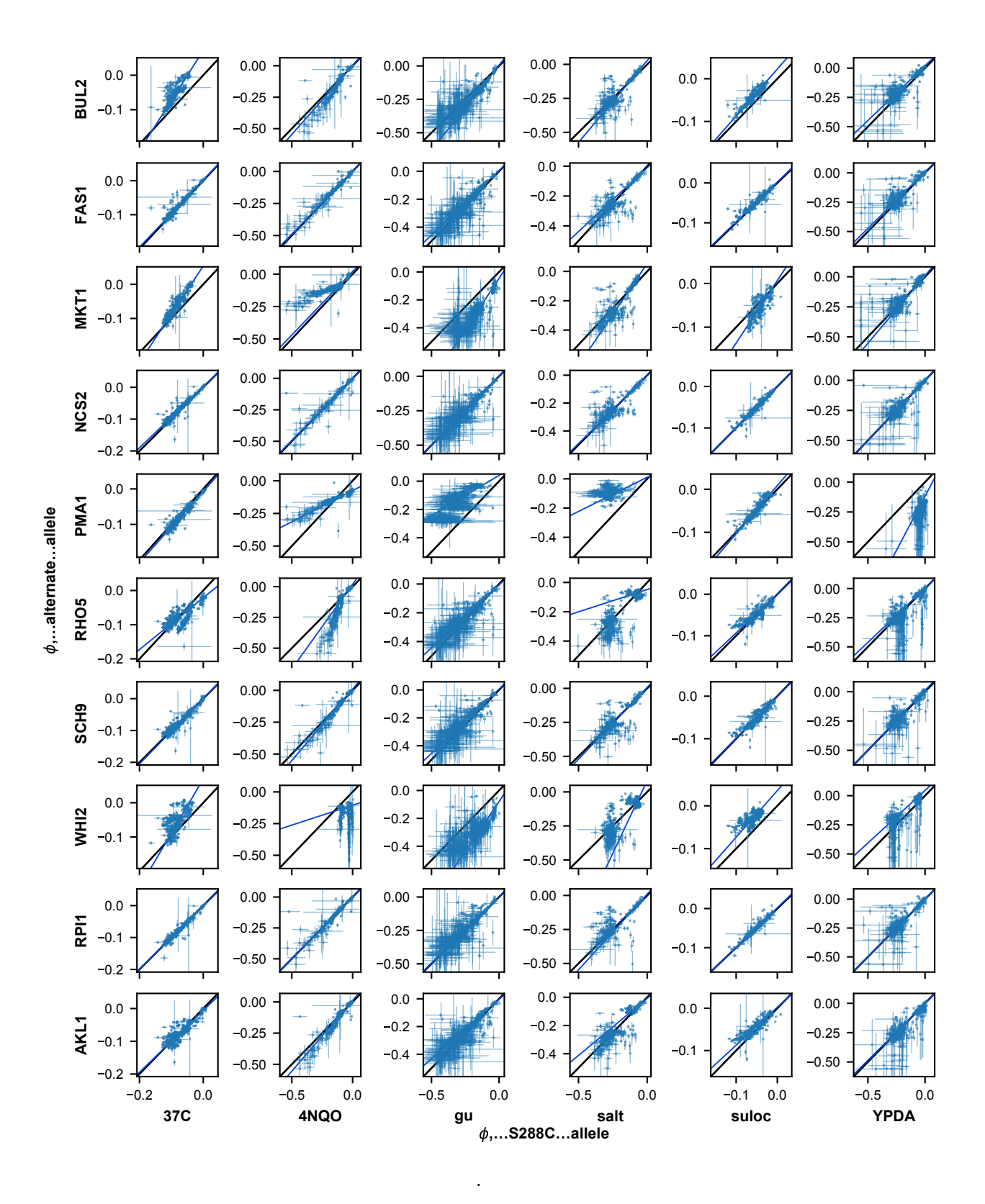


Figure S13: Scatter plots of ϕ_{wt}/ϕ_{mut} for all loci in haploid form.

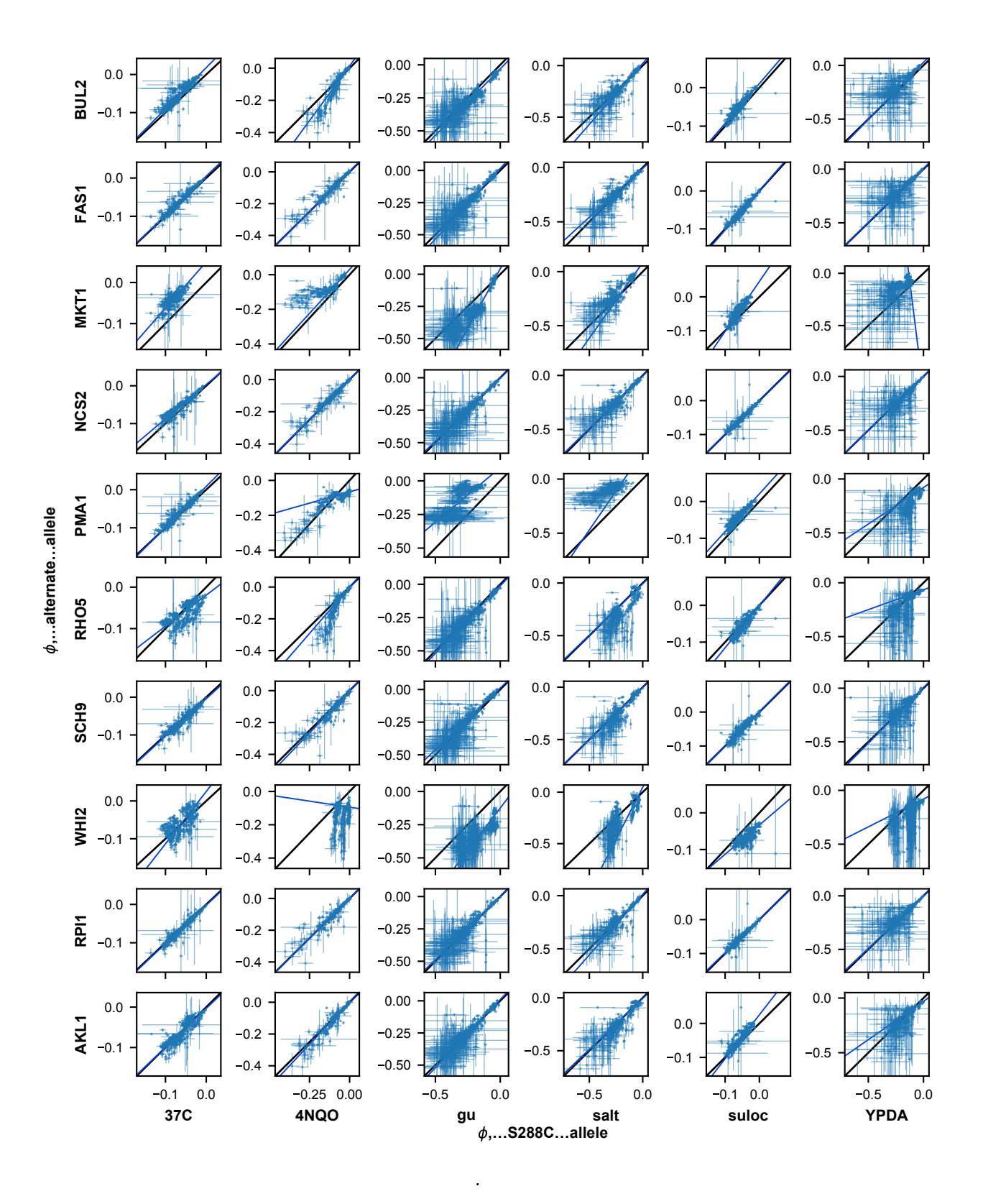


Figure S14: Scatterplots of ϕ_{wt}/ϕ_{mut} for all loci in homozygous form.

had the relevant idiosyncratic interactions, it may be possible to identify the relevant FCT in a smaller landscape. In general, however, because theory argues that it is the accumulation of many random idiosyncratic interactions that produces FCTs, we expect that larger landscapes become more likely to reveal this effect. By random, we mean that idiosyncratic interactions do not obey regular and predictable statistical patterns such as diminishing returns.

In addition to this, another key effect of landscape size is that the total number of genotypes, and hence the total number of fitness measurements, also increases exponentially with the number of mutations in the landscape. This reduces the influence of noise and improves our ability to identify FCTs and the potential effects of idiosyncratic interactions in producing them. This is critical, because linear regression analyses are known to be strongly affected by noise, which can produce outliers: the variance on the slope estimate is (roughly) inversely proportional to the number of data points used in the regression. Since increasing the number of loci considered in fitness landscapes leads to an exponential increase in the total number of data points, we expect that FCTs in significantly smaller landscapes (including landscapes like those examined in previous studies) would therefore be more affected by noise.

To explore these effects of landscape size on the decomposition of fitness-correlated trends (FCTs), we analyzed smaller sub-landscapes from the corresponding subsets of our data. By definition, we cannot disentangle the potential role of idiosyncratic epistasis in creating an FCT in a landscape consisting of only two loci. We therefore constructed landscapes with all possible subsets of three or more of our mutations. For each subset, we analyzed the potential FCT using our decomposition analysis (see Section 6.2). Specifically, for all subsets and all mutations that had evidence of FCT in the full-dataset (i.e., $b \le 0.9$), we computed the final ratio of sum-squared errors (SSE) between a model with a slope of 1 (this is the idiosyncratic FCT model) and a model with the global initial slope (the global FCT model), after removing all relevant epistatic terms. The idiosyncratic model is supported when this final ratio is below 1. Note that we excluded from this analysis subsets and mutations for which regressions were based on just 1 or 2 points.

We find that, at smaller subset sizes, there is a wide range of final relative fit ratios, indicating that the same mutation can be found to display evidence for either the idiosyncratic model or the global epistasis model driving FCTs. This spread of final SSE ratio can be explained by the random effects of which mutations happen to be represented in each subset, as well as the increased influence of noise on regression and on the inference of coefficients. However, we find that as the subset size increases, the range narrows, with most relative fit ratios dropping below 1 (Figure S15 and Figure S16). This indicates that noise is particularly important in determining whether we can distinguish between the idiosyncratic epistasis model and the global epistasis model, with smaller subsets containing exponentially fewer points and hence far fewer measurements of the fitness effect of mutations (or epistatic terms) with which to perform inference and regression. For our data, with sparse interactions, a landscape of size greater than 8 appears sufficient to provide strong support for the idiosyncratic model (Figure S15 and Figure S16).

To further confirm that noise is the primary driver of evidence towards the global epistasis model (i.e., toward a relative fit ratio > 1), we investigated cases where the final relative fit ratio remained above 1 even in our largest fitness landscapes. We found that these have a strong tendency to be mutations in environmental/ploidy combinations with the greatest evidence for noise as determined by the correlation between biological replicates (Figure S17). This suggests that these outstanding cases pointing to global epistasis would be resolved toward the idiosyncratic epistasis explanation with better measurements or with still larger landscapes. We also note that this finding suggests that apparent differences between environments (e.g. with salt and YPDA environments suggesting a larger role for global effects) may simply be an artifact of the inherently noisier fitness measurements in these conditions. These lines of analysis also suggest that previous studies

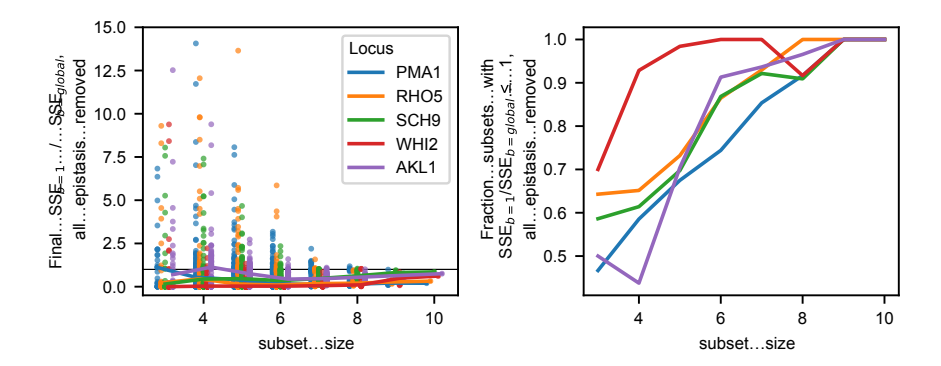


Figure S15: Effects of landscape size on the final SSE ratio (with values less than 1 indicating that FCTs are resolved in terms of idiosyncratic interactions) in 4NQO (haploid). In left panel, each point represents a subset of the full landscape of the corresponding size, with a particular focal mutation (indicated by the legend) having a fitness-correlated slope of $b \le 0.9$ (polarity adopted such that b is ≤ 1). The relative fit (sum-squared error, SSE) ratio between regressions with fixed slope of b=1 and b=global was computed after all epistatic terms were removed. At right, we show the fraction of subsets that have a final (all epistasis removed) relative fit ratio lower than 1 for each mutation, indicating support for the idiosyncratic model of fitness-correlated trends. Not shown are 16 points for which relative fit ratio is greater than 10. Lines show median ratios for each mutation.

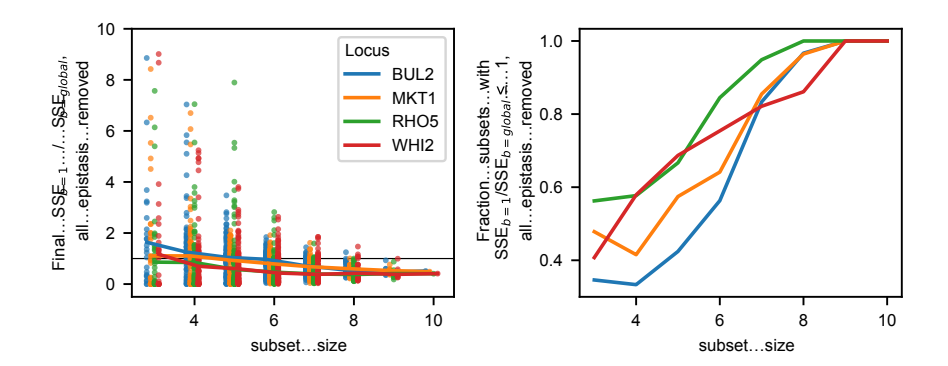


Figure S16: Effects of landscape size on the final SSE ratio (with values less than 1 indicating that FCTs are resolved in terms of idiosyncratic interactions) in 37C (haploid). In left panel, each point represents a subset of the full landscape of the corresponding size, with a particular focal mutation (indicated by the legend) having a fitness-correlated slope of $b \le 0.9$ (polarity adopted such that b is ≤ 1). The relative fit (sum-squared error, SSE) ratio between regressions with fixed slope of b=1 and b=global was computed after all epistatic terms were removed. At right, we show the fraction of subsets that have a final (all epistasis removed) relative fit ratio lower than 1 for each mutation, indicating support for the idiosyncratic model of fitness-correlated trends. Not shown are 15 points for which relative fit ratio is greater than 10. Lines show median ratios for each mutation.

with smaller landscape sizes might not have been able to decompose FCTs as being driven by idiosyncratic epistasis.

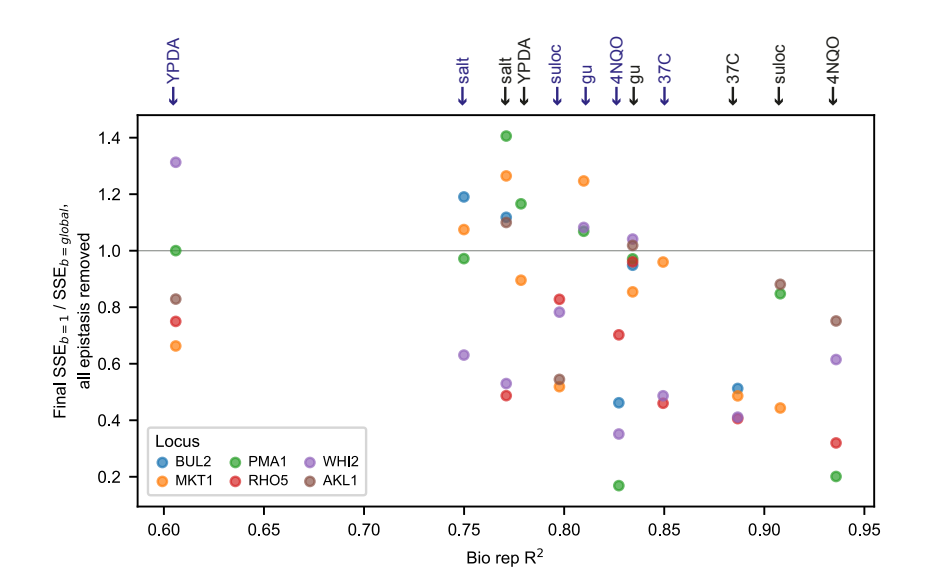


Figure S17: Final relative fit ratio as a function of reproducibility in biological replicates (i.e. the noise in individual fitness measurements). Each point represents the final sum-squared error ratio (i.e. the relative SSE ratio between regressions with a fixed slope of b=1 and b=global) for a given focal mutation (as indicated in legend) and environment (as indicated by arrows above, with haploids in black and homozygous diploids in blue). Note that SSE ratios greater than 1, which correspond to evidence for global epistasis, occur more frequently when the data is noisier. Only loci exhibiting an FCT in at least 3 of the 12 ploidy/environment combinations are presented.

765 7 Captions for Data Tables

₆ 7.1 Data Table S1

Primers used in genotyping, as well as search sequences used in parsing genotypes.

58 7.2 Data Table S2

769

770

771

772

773

774

775

776

Barcode to well to genotype map, and measured competitive fitness of each barcode in each ploidy and each environment.

The fitness values provided are joint inferred fitnesses from two technical replicates (two separate fitness assays were performed simultaneously), and the standard error is of the estimate is obtained from the effect of an overdispersed binomial sampling error on this estimate (see Section 4.3 for more details). The estimated starting frequency of the barcode in the fitness assay in each technical replicate is also provided.

The HSL7-SPT7-FRS1 worksheet indicates whether each well was pure for one or the other allele, or considered impure at a stated threshold.

7.3 Data Table \$3

Model parameters for each ploidy in each environment. We provide bootstrap 95% confidence intervals for the parameters as well.